

Nematicity and Orbital Depairing in Superconducting Bernal Bilayer Graphene with Strong Spin Orbit Coupling

Ludwig Holleis,¹ Caitlin L. Patterson,¹ Yiran Zhang,^{2,3,4} Yaar Vituri,⁵ Heun Mo Yoo,¹ Haoxin Zhou,^{1,3} Takashi Taniguchi,⁶ Kenji Watanabe,⁷ Erez Berg,⁵ Stevan Nadj-Perge,^{2,3} and Andrea F. Young^{1,*}

¹*Department of Physics, University of California at Santa Barbara, Santa Barbara CA 93106, USA*

²*T. J. Watson Laboratory of Applied Physics, California Institute of Technology,
1200 East California Boulevard, Pasadena, California 91125, USA*

³*Institute for Quantum Information and Matter, California Institute of Technology, Pasadena, California 91125, USA*

⁴*Department of Physics, California Institute of Technology, Pasadena, California 91125, USA*

⁵*Department of Condensed Matter Physics, Weizmann Institute of Science, Rehovot 76100, Israel*

⁶*International Center for Materials Nanoarchitectonics,*

National Institute for Materials Science, 1-1 Namiki, Tsukuba 305-0044, Japan

⁷*Research Center for Functional Materials, National Institute for Materials Science, 1-1 Namiki, Tsukuba 305-0044, Japan*

(Dated: June 13, 2024)

Superconductivity (SC) is a ubiquitous feature of graphite allotropes, having been observed in Bernal bilayers[1], rhombohedral trilayers[2], and a wide variety of angle-misaligned multilayers[3–6]. Despite significant differences in the electronic structure across these systems, supporting the graphite layer on a WSe₂ substrate has been consistently observed to expand the range of SC in carrier density and temperature[7–10]. Here, we report the observation of two distinct superconducting states (denoted SC₁ and SC₂) in Bernal bilayer graphene with strong proximity-induced Ising spin-orbit coupling. Quantum oscillations show that while the normal state of SC₁ is consistent with the single-particle band structure, SC₂ emerges from a nematic normal state with broken rotational symmetry. Both superconductors are robust to in-plane magnetic fields, violating the paramagnetic limit; however, neither reach fields expected for spin-valley locked Ising superconductors. We use our knowledge of the Fermi surface geometry of SC₁ to argue that superconductivity is limited by orbital depairing arising from the imperfect layer polarization of the electron wavefunctions. Finally, a comparative analysis of transport and thermodynamic compressibility measurements in SC₂ shows that the proximity to the observed isospin phase boundaries, observed in other rhombohedral graphene allotropes, is likely coincidental, constraining theories of unconventional superconducting pairing mechanisms in these systems.

Spin-orbit coupling (SOC) preserves the time reversal symmetry of electron bands in solids. As a result, SOC is not necessarily detrimental to the superconducting transition temperature: Cooper pairs may still condense from the degenerate Kramers' doublets by the same attractive interactions that lead to superconductivity in its absence[11, 12]. Within a weak-coupling Bardeen-Cooper-Schrieffer picture, SOC may either raise or lower the density of states with opposite consequences for T_c . However, SOC does typically make superconductors more resilient to applied magnetic fields by pinning the spin direction of electrons. One example is Ising

superconductivity[13–15], where in-plane mirror and time reversal symmetry protects Cooper pairs[16] making them, in theory, immune to arbitrarily large applied in-plane magnetic fields at zero temperature. Experimentally, however, other effects which break these symmetries will typically limit the critical in-plane magnetic field.

Graphene[1–6, 17–19] provides a unique venue to investigate the interplay of superconductivity and spin-orbit coupling. Due to the small atomic number of carbon, the atomic SOC in graphene is small[20, 21]. However, SOC may be induced by supporting the graphene layers on a transition metal dichalcogenide substrate such as WSe₂[22–29]. The existing literature appears to show a systematic enhancement of superconducting transition temperatures for graphene systems with induced spin-orbit coupling. For example, twisted bilayer and trilayer graphene on WSe₂ substrates was observed to superconduct for a wider range of angles[7, 9], while in twisted double bilayer graphene [30–34] superconductivity has been observed *only* on WSe₂ substrates[10]. However, the lack of reproducibility in graphene moiré systems[35] makes controlled experiments difficult.

Recently, it was shown that supporting Bernal bilayer graphene (BBG) on a WSe₂ substrate increases the maximal superconducting T_c by an order of magnitude and dramatically expands the domain of carrier density and applied electric displacement field over which superconductivity is observed[8]. BBG is an ideal candidate to quantitatively study the effect of proximity induced SOC on superconductivity. First, the magnetic and superconducting phase diagram of hexagonal boron nitride supported BBG is highly reproducible[1, 36], allowing for reliable experimental controls for the effects of SOC. Second, the magnitude of the proximity-induced Ising SOC can be precisely determined *in situ* using Landau level coincidences[37]. Finally, the simplicity of the BBG band structure allows for detailed comparisons between experiment and theoretical calculations. While prior experiments have found significant violations of the Pauli limit, the origin of the ultimate destruction of superconductivity in in-plane field has not been resolved, with both orbital

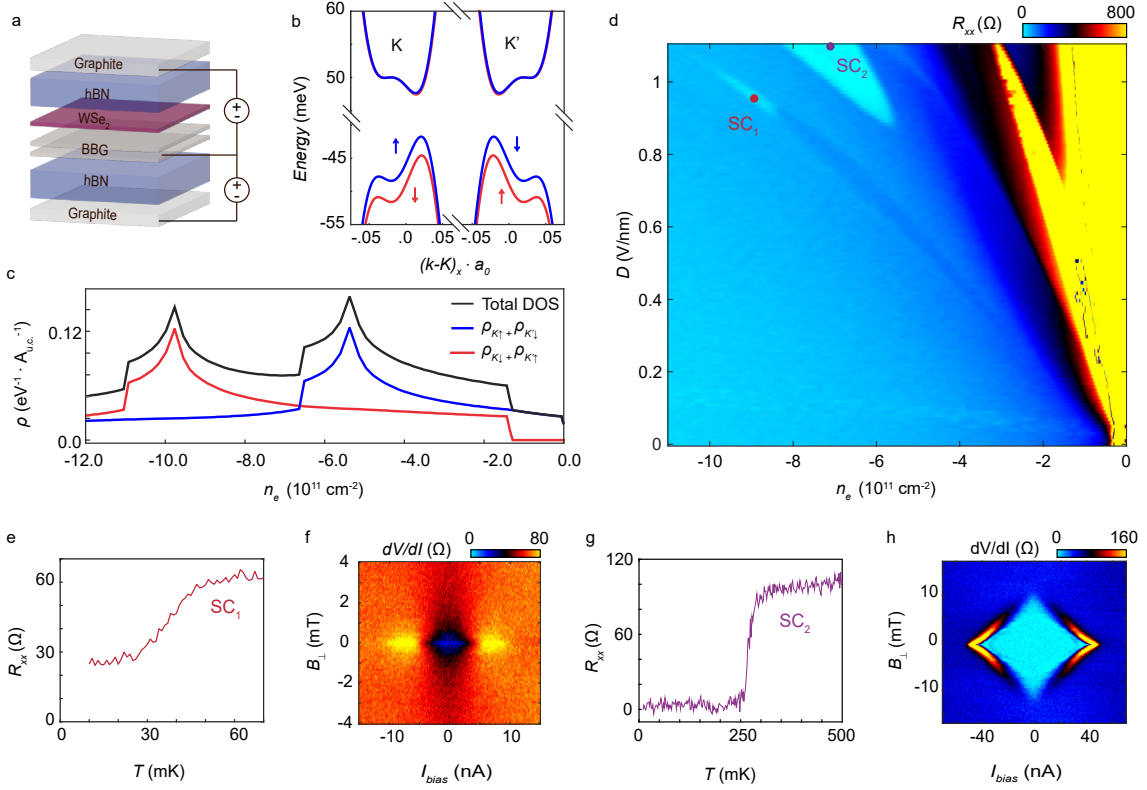


FIG. 1. Superconductivity in Bernal bilayer graphene (BBG) on WSe₂. (A) Sample schematic showing dual gated BGG on WSe₂. (B) Band structure calculated within a tight binding model including Ising SOC. Bands correspond to the different isospin flavors as indicated. Here $a_0 = 2.46 \text{ \AA}$ is the graphene lattice constant. (C) Total density of states (black) along with individual contributions from the spin/valley split bands, plotted for $D \approx 1.0 \text{ V/nm}$. (D) Longitudinal resistivity for hole-doped BGG/WSe₂. Two superconducting phases SC₁ and SC₂ are marked. (E) Temperature dependent resistivity of SC₁ at the point indicated by the red dot in panel D. (F) Perpendicular magnetic field B_{\perp} and current bias I_{bias} dependence at the same point. (G) Temperature dependent resistivity for SC₂ at the point indicated by the purple dot in panel D. (H) B_{\perp} and I_{bias} dependence at the same point.

effects and Rashba spin-orbit coupling possibly playing a role.

Here, we study a WSe₂-supported Bernal bilayer graphene device (Fig. 1A) with a measured proximity-induced Ising spin orbit coupling $\lambda_I = 1.6 \text{ meV}$ (see Fig. S1). We focus on hole filling and applied electric displacement fields $D > 0$. In this regime, electronic states near the Fermi energy are polarized on the layer adjacent to the WSe₂[8, 37]. Fig. 1B shows the low energy band structure calculated within a tight binding model[38] for an inter-layer potential of 100 meV, which corresponds to a displacement field $D \approx 1 \text{ V/nm}$ [39]. In the low density regime of $|n_e| < 10^{12} \text{ cm}^{-2}$, the measured Ising SOC is comparable to the Fermi energy, breaking the the native four-fold degeneracy of the spins and valleys and leaving a two-fold degeneracy between pairs of spin-valley locked bands. As shown in Fig. 1C, for $\lambda_I = 1.6 \text{ meV}$ the single-particle density of states is characterized by two well-separated van-Hove singularities, corresponding to the saddle points in each degenerate pair of spin/valley locked bands. Absent Ising SOC, the density of states of regular BGG displays only one van-Hove singularity[1].

Fig. 1D shows electrical transport measurements for low hole densities and as a function of displacement field. For

large displacement fields, we find two distinct superconducting states which we refer to as SC₁ and SC₂. SC₁ has a transition temperature $T_c \approx 40 \text{ mK}$, just above the base temperature of our dilution refrigerator. As a result the resistance does not reach zero, showing a saturation at the lowest temperatures (Fig. 1E) that we attribute to disequilibrium of the electron system with the phonon bath (see also Fig. S14). However, nonlinear transport measurements in an applied perpendicular magnetic field (Fig. 1F) show both strong non-linearities at sub-10 nA currents and exceptional magnetic field sensitivity characteristic of low- T_c superconductors in crystalline graphene systems[1, 2]. As shown in Fig. 1G, SC₂ has a much higher maximum transition temperature. By fitting the non-linear voltage to a Berezinskii–Kosterlitz–Thouless model [40, 41], we find $T_{BKT} \approx 255 \text{ mK}$ (Fig. S2). The B_{\perp} dependence shows a critical field of $B_C \approx 10 \text{ mT}$ (Fig. 1H), in line with previous reports of superconductivity in this regime[8].

To understand the normal phases from which these superconducting states condense, we perform high-resolution Shubnikov-de-Haas oscillation measurements, from which we resolve fine details of the Fermi surfaces. Fig. 2A, B show

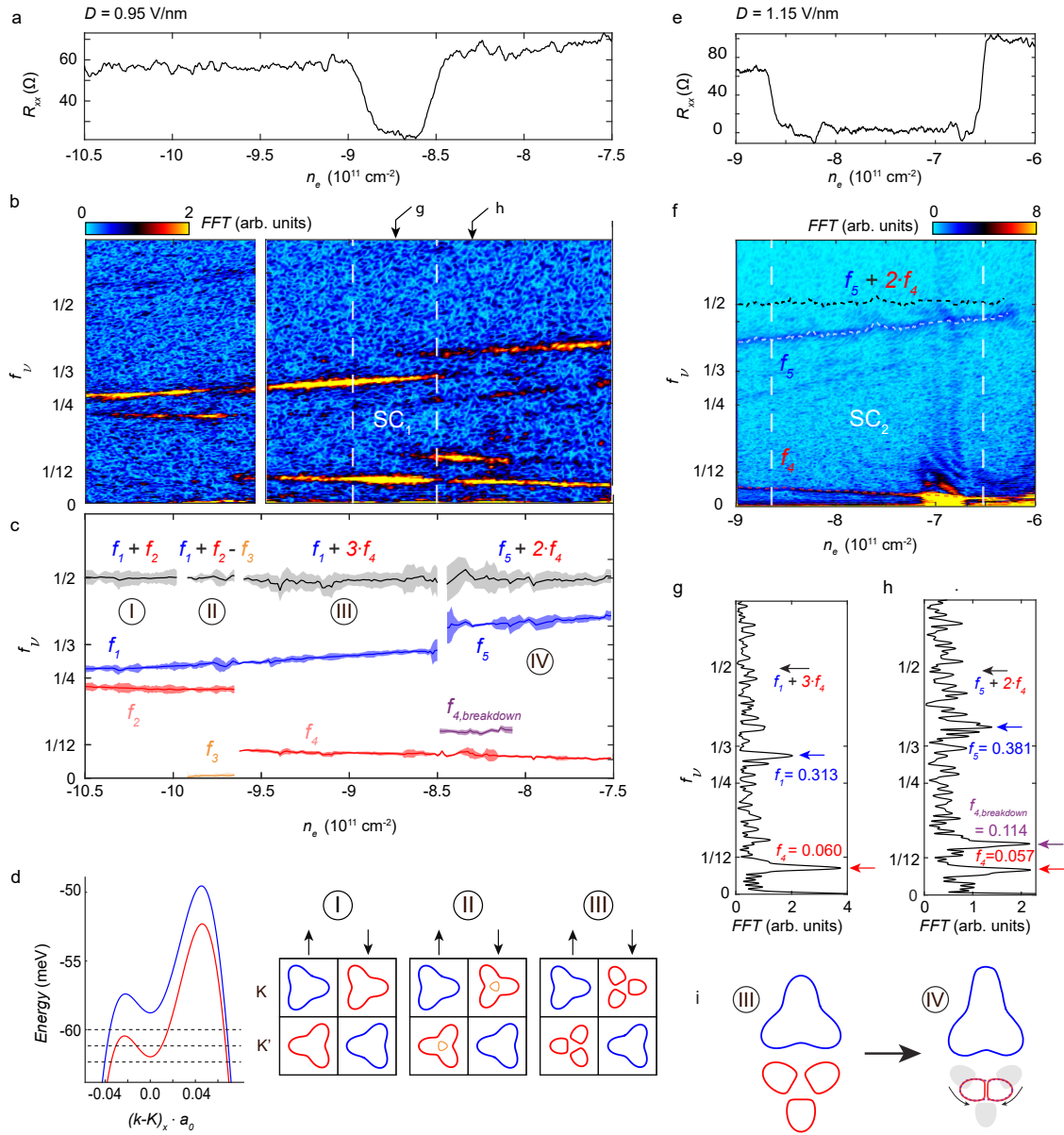


FIG. 2. Fermiology of the superconducting states in the presence of Ising SOC. (A) R_{xx} at $D = 0.95$ V/nm, including the domain of SC_1 . (B) Fourier transform of $R_{xx}(1/B_{\perp})$ over the same density range. The Fourier transforms are performed over a field range of 130 - 400 mT and 130 - 260 mT in the left and right panels, respectively (see Fig. S3 and SI). f_{ν} denotes the oscillation frequency normalized to the Luttinger volume, as described in the main text. (C) Intensity peaks in f_{ν} from panel B. Shaded areas represent error bars corresponding to the standard deviation of Gaussian fits to the peak frequencies. The black lines show the indicated frequency sums, providing a visual representation of the sum rules according to Eq. (1) described in the main text. (D) Single-particle band structure near the K point. The spin orbit split energy bands generate contrasting Fermi-surfaces for different spin-valley combinations, as shown in insets I, II, and III. (E) R_{xx} at $D = 1.15$ V/nm, including the domain of SC_2 . (F) f_{ν} corresponding to the n_e and D of panel E. Dashed lines show the peak fits and the sum rule. (G) Fourier transform amplitude of data in panel B for $n_e = -8.75 \cdot 10^{11} \text{ cm}^{-2}$ and (H) $n_e = -8.3 \cdot 10^{11} \text{ cm}^{-2}$. The peak positions are indicated, illustrating the quantitative agreement of the contrasting sum rules. (I) Schematic depiction of the nematic transition, in which one of the small Fermi pockets is absorbed by the large Fermi pocket with opposite spin and valley.

a comparison between zero magnetic field transport and the quantum oscillation frequencies f_{ν} at $D = 0.95$ V/nm, across the domain of SC_1 . Here, f_{ν} denotes the quantum oscillation frequency normalized to the total carrier density. f_{ν} thus represents the fraction of the total Luttinger volume encircled by

a given phase coherent orbit in momentum space. In these units, Luttinger's theorem may be expressed as

$$\sum_i k_i \cdot f_i = 1 \quad (1)$$

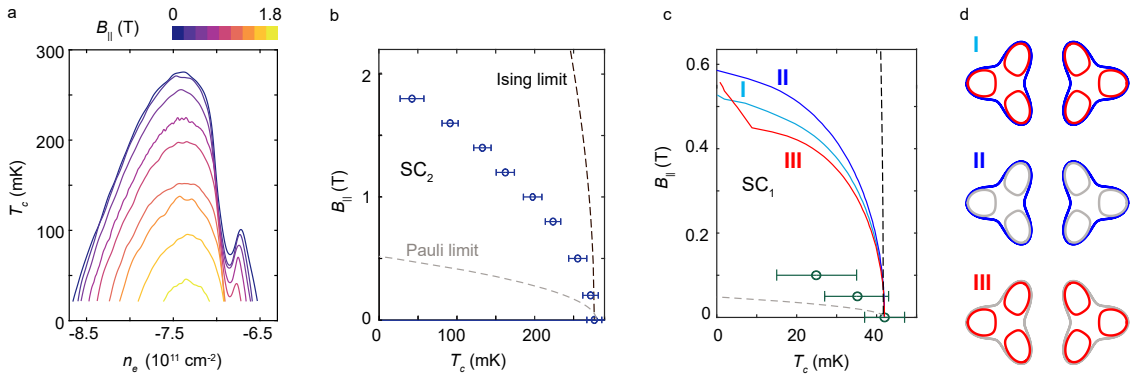


FIG. 3. **Orbital depairing from in-plane critical fields:** (A) Superconducting transition temperature for different values of B_{\parallel} for SC_2 at $D = 1.15$ V/nm. T_c is extracted from temperature dependent resistance data (see Fig. S6, S7) by defining $R(T_c)$ as half of the normal state resistance. (B) T_c as a function of B_{\parallel} for SC_2 for the maximum of the T_c domes in A. The black and grey dashed line represent the pure Ising superconductivity and Pauli limits, respectively. (C) The same plot for SC_1 where the bandstructure is in the approximate single particle limit known from quantum oscillations (see 2). The three solid lines represent the calculated in-plane critical fields including orbital depairing. Each line I-III represents a different subset of Fermi pockets hosting superconductivity as illustrated in D. (D) shows the single particle Fermi surfaces used to determine the in-plane orbital effect in C. For I, II, III all Fermi pockets, only the large and only the three small pockets in each valley are included in the calculation, respectively. Fermi surfes not contributing to superconductivity are greyed out.

where the index i runs over all peaks corresponding to single orbits of a Fermi surface and k_i is an integer degeneracy and carrier sign for the Fermi surfaces producing the oscillation at frequency f_i .

Fig. 2C distills the data of Fig. 2B by plotting only the center frequencies and standard deviations extracted from Gaussian fits of the observed peaks. Across the density range corresponding to regions I, II, and III, the oscillation frequencies can be understood from the SOC-modified single-particle band structure of Fig. 1B-C. For example, region I shows two peaks with slightly different frequencies, denoted f_1 and f_2 , where $f_1 + f_2 = 1/2$ within experimental error. Using Eq.1, we see that Luttinger’s theorem may be satisfied by assigning a two fold degeneracy to both Fermi surfaces, $k_1 = k_2 = 2$. As shown in Fig. 2D, this is consistent with SOC-modified band structure where the favored- and disfavored spin-valley locked bands have slightly mismatched Fermi surface areas even at comparatively high densities. We denote this state $Ising_{2,2}$. In region II, we observe the emergence of an additional peak, f_3 . Due to its low frequency, f_3 is barely visible in Fig. 2B but can clearly be identified in the raw resistance and capacitance measurements (see Fig. S3). This is again consistent with band structure, and marks the formation of an annular Fermi sea with both hole-like and electron-like Fermi surfaces. The sum rule implied by the band structure model, $f_1 + f_2 - f_3 = 1/2$ is again consistent with experimental data, and we denote this state $Ising_{2,2,-2}$. In region III, both f_2 and f_3 vanish and are replaced by a peak at intermediate frequency f_4 . The Luttinger sum rule is satisfied for $k_1 = 2$ and $k_4 = 6$, as expected after the minority-occupation bands cross the saddle point and each annular Fermi sea breaks into three pockets. We label this state $Ising_{2,6}$, and conclude that SC_1 emerges from a normal state with no additional broken symmetries as compared to the single particle picture.

At the low- $|n_e|$ boundary of SC_1 , f_1 abruptly disappears and is replaced by a peak (f_5) at higher frequency and a peak at frequency $2 \cdot f_4$, while f_4 continues its linear trend. The fermiology of region IV is consistent across a large domain of n_e and D , including the entire domain of SC_2 , as shown in Figs. 2E, F for the highest accessible displacement field and in Fig. S5 at $D = 1.05$ V/nm for a larger density range. This is unexpected within the single particle picture, which cannot account for the emergence of a *larger* f_ν peak as $|n_e|$ is lowered.

As shown in Fig. S4, the peak at $2 \cdot f_4$ can be attributed to ‘magnetic breakdown’[42] between the Fermi surfaces represented by f_4 , and we denote it $f_{4,breakdown}$; as a result, it should not be counted towards the sum rule of Eq.(1). Remarkably, among simple possibilities, Luttinger’s theorem is satisfied only for $k_5 = 2$ and $k_4 = 4$ (Fig. 2G, H). This assignment implies that for a single spin-valley flavor in a minority band, the Fermi surface degeneracy is 2—a fact plainly incompatible with preserving the C_3 point group symmetry of bilayer graphene. We conclude that the parent state of SC_2 , and adjoining state to SC_1 , is nematic and we denote it $N_{2,4}$. Notably, most prior experiments probing possible nematicity in graphene devices[9, 43–46] have focused on resistance anisotropy. These measurements rely on structural uniformity of the device, a condition that can be difficult to meet under realistic experimental conditions in mesoscopic two dimensional samples. Because quantum oscillations probe closed electron orbits in the sample bulk they provide a detection scheme for nematic order that is immune to many of these possible sources of systematic error. Of course, the Fermi surface degeneracy is not directly sensitive to nematic order, producing ‘false negatives’ when its topology is compatible with C_3 symmetry. However, in the case studied here, quantum oscillations provide unambiguous evidence for a nematic ground

state.

Incidentally, attributing region IV to a nematic phase provides a natural explanation for the observation of the magnetic breakdown peak $f_{4,breakdown}$. Breaking C_3 symmetry relaxes the requirement that the small Fermi pockets be arranged symmetrically around the K and K' points. In this picture, the two small pockets remaining in the $N_{2,4}$ phase may move in momentum space to balance the competing effects of the kinetic and exchange contributions to the total energy; Fig. 2I illustrates a schematic representation of the fermiology in the $N_{2,4}$ phase near the III-IV transition where the pockets are very close, enabling breakdown. As the density is tuned deeper into region IV, the breakdown signal at $2 \cdot f_4$ fades, implying that the pockets eventually decouple, growing farther apart in momentum space as they shrink in relative volume.

Theoretically, a variety of nematic phases have been proposed throughout the phase diagrams of Bernal and rhombohedral graphene[8, 47–53]. These include phases with differing isospin orders, including phases that conserve the occupation of the two valleys separately and those that develop inter-valley coherence[8, 50, 51, 54, 55]. While quantum oscillations cannot distinguish these states directly, the phenomenology of SC_2 , which develops in the $N_{2,4}$ phase, allows us to rule out at least some possibilities.

Next, we study the in-plane critical field dependence of both superconductors. Fig. 3A shows T_c as a function of the in-plane magnetic field, B_{\parallel} , at $D = 1.15$ V/nm for SC_2 . In Fig. 3B, we contrast the B_{\parallel} dependence of the maximal experimental T_c with two limits. The paramagnetic (“Pauli”) limit for a spin-singlet superconductor is determined by the competition between the Zeeman energy and the pairing gap (proportional to the transition temperature), $\mu_B B_P = 1.23k_B T_{c,0}$ [56, 57]. For large Ising SOC (the “Ising” limit), in contrast, superconductivity is almost impervious to the in-plane Zeeman energy[13] as long as the Zeeman energy is much smaller than the spin orbit coupling. In these systems, superconductivity consists of both spin singlet and spin-triplet components, with the latter becoming more dominant as the electron spins cant in an applied in-plane magnetic field.

Our experimental data fall between these two limits. This raises the question of which of several possible mechanisms—including Rashba spin orbit coupling, disorder, and the orbital effect of the in-plane field[8, 15, 16]—limit superconductivity at high B_{\parallel} . To address this question, we focus on SC_1 , which also shows a B_{\parallel} dependent critical temperature intermediate between the Pauli and Ising limits (see Fig. 3C). In contrast to other superconducting states observed in Bernal bilayer graphene, however, the fermiology of the normal state of SC_1 extracted from quantum oscillation measurements is well fit by a single particle band structure model (See Fig. S16). This implies that Coulomb interactions induce only moderate Fermi surface renormalization in this regime. We may thus take a single particle band structure model as a basis to esti-

mate pair breaking effects. To model the pair-breaking effect of the in-plane magnetic field, we set $\vec{A} = z(\vec{B} \times \hat{z})$ and perform a Peierls substitution to extract the magnetic field dependent band structure. We take a linear approximation of the dispersion in \vec{B} and in the momentum perpendicular to the Fermi surface and solve the linearized gap equation to find T_c as a function of B_{\parallel} . As shown in Figure 3C, including the orbital effect of B_{\parallel} lowers the critical magnetic field from $B \approx 10T$ at low temperatures to $B_{\parallel} \approx 500mT$, accounting for the bulk of the discrepancy with the experimental data. Rashba spin-orbit coupling induced by the WSe_2 substrate may also be included within this model; for Rashba coupling constant as large as $\lambda = 2$ meV, we find that it has negligible effect on T_c due to the sublattice polarization of the electronic states near the Fermi level (see fig. S17). Notably, although the dispersion and the orbital moment are not symmetric to in-plane rotations, we find numerically that T_c is only weakly dependent on the direction of B_{\parallel} in the plane, consistent with a lack of detectable experimental dependence on the angle between B_{\parallel} and the graphene lattice vectors. This leaves the question of the origin of the remaining quantitative discrepancy between the experimental data and our model. One source of systematic error is experimental: the low values of T_c will be affected by the disequilibrium between the charge carriers with the phonon bath, which tends to decrease measured T_c relative to its true value.

An additional discrepancy may arise from the fact that quantum oscillations measure only the Fermi surface pocket size and number, but not their position. Coulomb-induced Fermi surface reconstructions may change the positions of the Fermi pockets—and thus the in-plane orbital moment of states at the Fermi surface—without noticeable changes to fermiology inferred from quantum oscillations. To investigate the possible magnitude of this effect, we compare three models for superconducting pairing (see Fig. 3C-D) based on the Fermi surfaces calculated from the single-particle band structure. These assume superconducting pairing within all, only the large, or only the small Fermi pockets. These different assumptions produce a range of low temperature critical B_{\parallel} of $\sim 150mT$, despite the close proximity in momentum space of the different Fermi pockets. It seems likely, then, that additional Fermi surface reconstruction may be sufficient to close the gap between theory and experiment.

We conclude that orbital effects are the dominant source of depairing in in-plane magnetic fields. Notably, this effect applies to both the Ising-enhanced and spin-triplet superconductors in graphene: the contrasting in plane orbital magnetic moments in the two valleys provide a source of pair breaking in a magnetic field for any superconductor in which pairing occurs between states at the two corners of the Brillouin zone. This finding implies that detailed knowledge of the Fermi surface is essential for interpreting the in-plane critical field in multi-layer graphene superconductors—besides violations of the Pauli limit, the upper critical field may not provide any information on the spin structure of the condensate. Rather, Pauli limit violations may provide information about the mo-

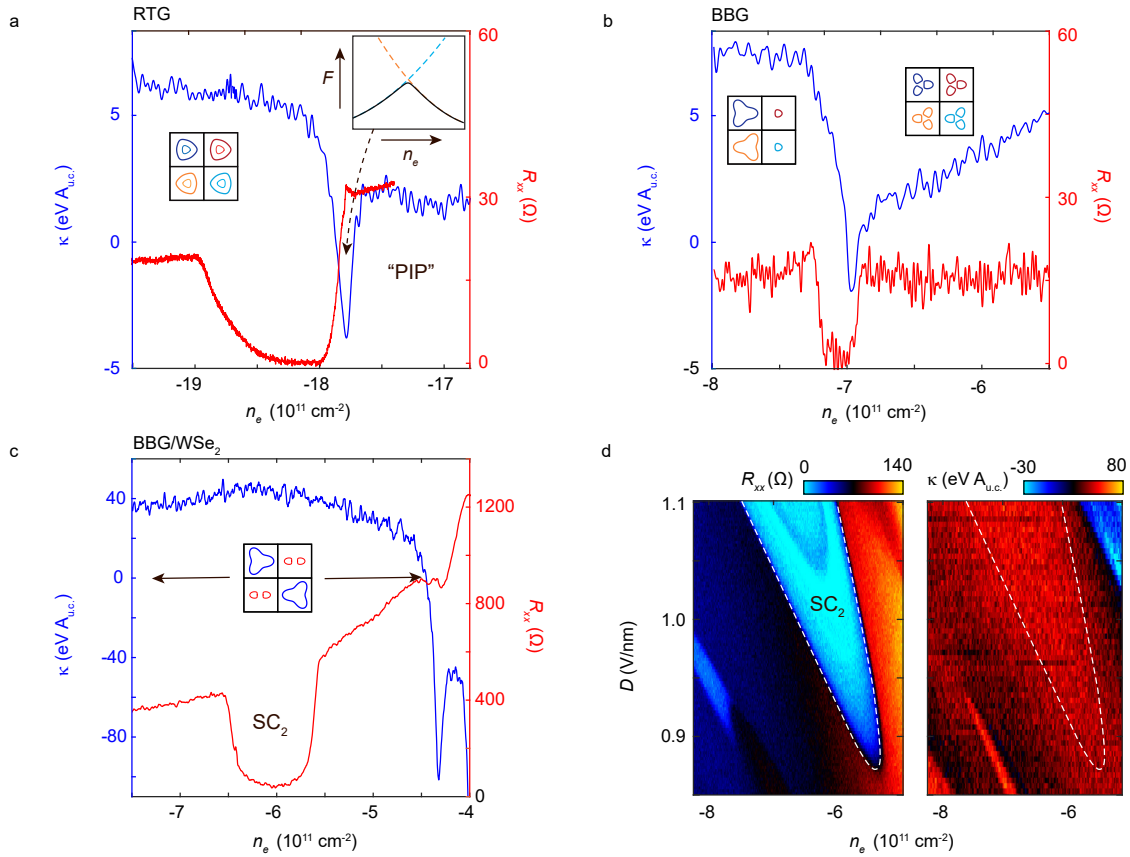


FIG. 4. **Superconductivity and thermodynamic phase transitions in crystalline graphene superconductors.** (A) Resistivity R_{xx} and inverse compressibility $\kappa = \partial\mu/\partial n_e$ in rhombohedral trilayer graphene (RTG) for $D = 0.46$ V/nm and $T \approx 60$ mK[2]. The lower inset illustrates the fermiology as described in [2], while the upper inset depicts a schematic of the free energy (black line) across a first order phase transition. As $\kappa = \partial^2 F/\partial n_e^2$, inverse compressibility is strongly negative at the transition. (B) R_{xx} and κ for BBG, measured at $D = 1.04$ V/nm and $B_{\parallel} = 400$ mT. Insets depict fermiology as described in [1]. (C) R_{xx} and κ for SC₂ in BBG/WSe₂ at $D = 0.95$ V/nm taken at $T \approx 20$ mK. The N_{2,4} phase spans nearly the entire range of the plot. (D) R_{xx} (left) and κ (right) measured over a range of n_e and D . The superconducting dome is overlaid from the transport onto the inverse compressibility map via the white dashed line.

momentum space positions of the Fermi surfaces involved in superconducting pairing. For example, both rhombohedral trilayer and BBG/WSe₂ devices[2, 8] have shown Pauli limit violations that become largest before the system undergoes a phase transition; this may imply that pairing between states is occurring closer to the Brillouin zone corners, where the wave functions are most layer polarized.

Lastly, we contrast superconductivity in BBG/WSe₂ with crystalline graphene superconductors without proximity induced SOC. In these systems, superconductivity has been observed only near isospin phase transitions[1, 2]. However, the nature of these transitions has not been experimentally determined. To characterize the phase transitions and their connection to superconductivity, we measure both resistance and the inverse electronic compressibility $\kappa = \partial\mu/\partial n_e$. We take pains to measure these simultaneously, ensuring that compressibility measurements are taken under identical conditions, and do not heat the electron systems (see Fig. S15 and Methods). Fig. 4A shows the comparison of R_{xx} and κ for rhombohedral trilayer (RTG). The isospin transition be-

tween the isospin unpolarized state and the partially isospin polarized state (PIP) is first order, as indicated by the negative compressibility peak (see Fig. 4A inset) observed at the phase boundary. In this regime, superconductivity is observed on the isospin-disordered side of the phase boundary. Fig. 4B shows the same comparison for BBG, taken in the high-D, high B_{\parallel} regime where triplet superconductivity is observed. Again, superconductivity occurs immediately adjacent to a first order phase transition, in this case on the isospin-ordered side.

In BBG/WSe₂, the evolution of the isospin polarization near SC₁ bears a superficial resemblance to these systems, with superconductivity developing adjacent to a phase boundary (Fig. S13). However, the phenomenology of SC₂ contrasts markedly: as illustrated in Fig. 4C, superconductivity emerges deep within the nematic N_{2,4} phase, far from any isospin phase transitions. This is corroborated by Fig. 4D, which compares transport and compressibility across a wide range of n_e and D ; the domain of superconductivity approaches a first order isospin transition only at the largest displacement fields, but is otherwise uncorrelated. The lack of direct cor-

relation between superconductivity and phase boundaries is also evident in the quantum oscillation data of Fig. 2F, where superconductivity develops, peaks, and subsides over a range for which fermiology evolves monotonically.

These observations suggest that the observed correlation between superconductivity and phase transitions in crystalline graphene layers is likely coincidental. Rather, superconductivity evolves within a given phase but may be destroyed if a competing phase with different symmetry becomes energetically favorable. Within this picture, the enhancement of superconductivity in WSe₂-supported graphene devices arises from the broken ‘spinless’ time reversal symmetry relating wavefunctions in opposite valleys with the same spin. Breaking this symmetry at the single-particle level preferentially stabilizes a subset of orders featuring two-particle states near the Fermi level compatible with Cooper pairing[11, 12]. It then becomes possible to trace the evolution of superconductivity within a single phase to its maximum strength. SOC may also suppress fluctuations of electronic orders which may suppress superconductivity[53, 55, 58–61]. In the case of the valley-symmetric nematic order depicted in Fig. 2I, n_e - and D -tuned details of the electron wavefunctions near the Fermi surface must then account for non-monotonic dependence of the transition temperature across the phase.

By breaking a symmetry not required for superconductivity (spinless time reversal), SOC stabilizes electronic orders with higher superconducting T_c , including nematic states. In the future, this procedure may be generalized, for example by applying uniaxial strain. Coupling of the strain to a nematic order parameter would then increase the range of stability of the $N_{2,4}$ phase, possibly further enhancing superconductivity.

Acknowledgements. The authors would like to acknowledge discussions with Maksym Serbyn, Areg Ghazaryan, A. H. MacDonald, Zhiyu Dong, Maxim Khodas, and Patrick A. Lee. The work was supported by the Office of Naval Research under award N00014-20-1-2609, and the Gordon and Betty Moore Foundation under award GBMF9471. Work at Caltech has been supported by the NSF-CAREER award (DMR-1753306). K.W. and T.T. acknowledge support from the Elemental Strategy Initiative conducted by the MEXT, Japan (Grant Number JPMXP0112101001) and JSPSKAKENHI (Grant Numbers 19H05790, 20H00354 and 21H05233). E.B. and Y.V. were supported by NSF-BSF award DMR-2310312 and by the European Research Council (ERC) under grant HQMAT (grant agreement No. 817799).

* andrea@physics.ucsb.edu

- [1] H. Zhou, L. Holleis, Y. Saito, L. Cohen, W. Huynh, C. L. Patterson, F. Yang, T. Taniguchi, K. Watanabe, and A. F. Young, *Science* **375**, 774 (2022).
- [2] H. Zhou, T. Xie, T. Taniguchi, K. Watanabe, and A. F. Young, *Nature* **598**, 434 (2021).
- [3] Y. Cao, V. Fatemi, S. Fang, K. Watanabe, T. Taniguchi, E. Kaxiras, and P. Jarillo-Herrero, *Nature* **556**, 43 (2018).
- [4] J. M. Park, Y. Cao, K. Watanabe, T. Taniguchi, and P. Jarillo-Herrero, *Nature* **590**, 249 (2021).
- [5] Y. Zhang, R. Polski, C. Lewandowski, A. Thomson, Y. Peng, Y. Choi, H. Kim, K. Watanabe, T. Taniguchi, J. Alicea, F. von Oppen, G. Refael, and S. Nadj-Perge, *Science* **377**, 1538 (2022).
- [6] J. M. Park, Y. Cao, L. Q. Xia, S. Sun, K. Watanabe, T. Taniguchi, and P. Jarillo-Herrero, *Nature Materials* **21**, 877 (2022).
- [7] H. S. Arora, R. Polski, Y. Zhang, A. Thomson, Y. Choi, H. Kim, Z. Lin, I. Z. Wilson, X. Xu, J.-H. Chu, K. Watanabe, T. Taniguchi, J. Alicea, S. Nadj-Perge, and Y. Zhang, *Nature* **583**, 379 (2020).
- [8] Y. Zhang, R. Polski, A. Thomson, E. Lantagne-Hurtubise, C. Lewandowski, H. Zhou, K. Watanabe, T. Taniguchi, J. Alicea, and S. Nadj-Perge, *Nature* **613**, 268 (2023).
- [9] J. X. Lin, P. Siriviboon, H. D. Scammell, S. Liu, D. Rhodes, K. Watanabe, T. Taniguchi, J. Hone, M. S. Scheurer, and J. I. Li, *Nature Physics* **18**, 1221 (2022).
- [10] R. Su, M. Kuiri, K. Watanabe, T. Taniguchi, and J. Folk, *arXiv* (2022), arXiv:2211.16449.
- [11] M. Sigrist, A. Avella, and F. Mancini, in *AIP Conference Proceedings*, Vol. 55 (AIP, 2009) pp. 55–96.
- [12] E. Bauer and M. Sigrist, eds., *Non-Centrosymmetric Superconductors*, Lecture Notes in Physics, Vol. 847 (Springer Berlin Heidelberg, Berlin, Heidelberg, 2012).
- [13] J. M. Lu, O. Zheliuk, I. Leermakers, N. F. Yuan, U. Zeitler, K. T. Law, and J. T. Ye, *Science* **350**, 1353 (2015).
- [14] X. Xi, Z. Wang, W. Zhao, J. H. Park, K. T. Law, H. Berger, L. Forró, J. Shan, and K. F. Mak, *Nature Physics* **12**, 139 (2016).
- [15] Y. Saito, Y. Nakamura, M. S. Bahramy, Y. Kohama, J. Ye, Y. Kasahara, Y. Nakagawa, M. Onga, M. Tokunaga, T. Nojima, Y. Yanase, and Y. Iwasa, *Nature Physics* **12**, 144 (2016).
- [16] D. Möckli and M. Khodas, *Physical Review B* **101** (2020), 10.1103/PhysRevB.101.014510, arXiv:1908.11662.
- [17] M. Yankowitz, S. Chen, H. Polshyn, Y. Zhang, K. Watanabe, T. Taniguchi, D. Graf, A. F. Young, and C. R. Dean, *Science* **363**, 1059 (2019).
- [18] Z. Hao, A. M. Zimmerman, P. Ledwith, E. Khalaf, D. H. Najafabadi, K. Watanabe, T. Taniguchi, A. Vishwanath, and P. Kim, *Science* **371**, 1133 (2021).
- [19] Y. Cao, J. M. Park, K. Watanabe, T. Taniguchi, and P. Jarillo-Herrero, *Nature* **595**, 526 (2021).
- [20] J. Sichau, M. Prada, T. Anlauf, T. J. Lyon, B. Bosnjak, L. Tieemann, and R. H. Blick, *Physical Review Letters* **122**, 46403 (2019).
- [21] T. Arp, O. Sheekey, H. Zhou, C. L. Tschirhart, C. L. Patterson, H. M. Yoo, L. Holleis, E. Redekop, G. Babikyan, T. Xie, J. Xiao, Y. Vituri, T. Holder, T. Taniguchi, K. Watanabe, M. E. Huber, E. Berg, and A. F. Young, (2023), arXiv:2310.03781.
- [22] A. Avsar, J. Y. Tan, T. Taychatanapat, J. Balakrishnan, G. K. Koon, Y. Yeo, J. Lahiri, A. Carvalho, A. S. Rodin, E. C. O’Farrell, G. Eda, A. H. Castro Neto, and B. Özyilmaz, *Nature Communications* **5**, 1 (2014).
- [23] Z. Wang, D. K. Ki, H. Chen, H. Berger, A. H. MacDonald, and A. F. Morpurgo, *Nature Communications* **6**, 1 (2015).
- [24] Z. Wang, D. K. Ki, J. Y. Khoo, D. Mauro, H. Berger, L. S. Levitov, and A. F. Morpurgo, *Physical Review X* **6**, 1 (2016).
- [25] B. Yang, M. Lohmann, D. Barroso, I. Liao, Z. Lin, Y. Liu, L. Bartels, K. Watanabe, T. Taniguchi, and J. Shi, *Physical Review B* **96**, 1 (2017).

- [26] T. Völkl, T. Rockinger, M. Drienovsky, K. Watanabe, T. Taniguchi, D. Weiss, and J. Eroms, *Physical Review B* **96**, 1 (2017).
- [27] S. Zihlmann, A. W. Cummings, J. H. Garcia, M. Kedves, K. Watanabe, T. Taniguchi, C. Schönenberger, and P. Makk, *Physical Review B* **97**, 1 (2018).
- [28] T. Wakamura, F. Reale, P. Palczynski, S. Guéron, C. Mattevi, and H. Bouchiat, *Physical Review Letters* **120**, 1 (2018).
- [29] D. Wang, S. Che, G. Cao, R. Lyu, K. Watanabe, T. Taniguchi, C. N. Lau, and M. Bockrath, *Nano Letters* **19**, 7028 (2019).
- [30] G. W. Burg, J. Zhu, T. Taniguchi, K. Watanabe, A. H. Macdonald, and E. Tutuc, *Physical Review Letters* **123**, 197702 (2019).
- [31] C. Shen, Y. Chu, Q. S. Wu, N. Li, S. Wang, Y. Zhao, J. Tang, J. Liu, J. Tian, K. Watanabe, T. Taniguchi, R. Yang, Z. Y. Meng, D. Shi, O. V. Yazyev, and G. Zhang, *Nature Physics* **16**, 520 (2020).
- [32] D. H. Najafabadi, K. Watanabe, T. Taniguchi, A. Vishwanath, and P. Kim, *Nature* **583** (2020), 10.1038/s41586-020-2458-7.
- [33] Y. Cao, T. Taniguchi, and P. Jarillo-herrero, *Nature* **583** (2020), 10.1038/s41586-020-2260-6.
- [34] M. He, Y. Li, J. Cai, Y. Liu, K. Watanabe, T. Taniguchi, X. Xu, and M. Yankowitz, *Nature Physics* **17** (2021), 10.1038/s41567-020-1030-6.
- [35] C. N. Lau, M. W. Bockrath, K. F. Mak, and F. Zhang, *Nature* **602**, 41 (2022).
- [36] S. C. de la Barrera, S. Aronson, Z. Zheng, K. Watanabe, T. Taniguchi, Q. Ma, P. Jarillo-Herrero, and R. Ashoori, *Nature Physics* **18**, 771 (2022).
- [37] J. O. Island, X. Cui, C. Lewandowski, J. Y. Khoo, E. M. Spanton, H. Zhou, D. Rhodes, J. C. Hone, T. Taniguchi, K. Watanabe, L. S. Levitov, M. P. Zaletel, and A. F. Young, *Nature* **571**, 85 (2019).
- [38] J. Jung and A. H. MacDonald, *Physical Review B* **89**, 035405 (2014).
- [39] Y. Zhang, T. T. Tang, C. Girit, Z. Hao, M. C. Martin, A. Zettl, M. F. Crommie, Y. R. Shen, and F. Wang, *Nature* **459**, 820 (2009).
- [40] V. L. Berezinskii, *Sov. Phys. JETP* **32**, 493 (1971).
- [41] J. M. Kosterlitz and D. J. Thouless, *J. Phys. C : Solid State Phys* **6** (1973).
- [42] W. Biberacher, *Encyclopedia of Condensed Matter Physics*, 360 (2005).
- [43] Y. Cao, D. Rodan-Legrain, J. M. Park, N. F. Yuan, K. Watanabe, T. Taniguchi, R. M. Fernandes, L. Fu, and P. Jarillo-Herrero, *Science* **372**, 264 (2021).
- [44] J.-X. Lin, Y. Wang, N. J. Zhang, K. Watanabe, T. Taniguchi, L. Fu, and J. I. A. Li, *arXiv*, 1 (2023), arXiv:2302.04261.
- [45] N. J. Zhang, Y. Wang, K. Watanabe, T. Taniguchi, O. Vafek, and J. I. A. Li, *arXiv*, 1 (2022), arXiv:2211.01352.
- [46] N. J. Zhang, J.-X. Lin, Y. Wang, K. Watanabe, T. Taniguchi, L. Fu, and J. I. A. Li, *arXiv*, 1 (2022), arXiv:2209.12964.
- [47] Y. Lemonik, I. L. Aleiner, C. Toke, and V. I. Fal'ko, *Physical Review B - Condensed Matter and Materials Physics* **82**, 1 (2010).
- [48] O. Vafek and K. Yang, *Physical Review B - Condensed Matter and Materials Physics* **81**, 1 (2010).
- [49] A. S. Mayorov, D. C. Elias, M. Mucha-Kruczynski, R. V. Gorbachev, T. Tudorovskiy, A. Zhukov, S. V. Morozov, M. I. Katsnelson, A. K. Geim, and K. S. Novoselov, *Science* **333**, 860 (2011).
- [50] Z. Dong, M. Davydova, O. Ogunnaike, and L. Levitov, *Physical Review B* **107**, 075108 (2023).
- [51] C. Huang, T. Wolf, W. Qin, N. Wei, I. Blinov, and A. MacDonald, *arXiv* (2022), arXiv:2203.12723.
- [52] A. L. Szabó and B. Roy, *Physical Review B* **105**, L201107 (2022).
- [53] J. B. Curtis, N. R. Poniatowski, Y. Xie, A. Yacoby, E. Demler, and P. Narang, *arXiv* (2022), arXiv:2209.10560.
- [54] S. Chatterjee, T. Wang, E. Berg, and M. P. Zaletel, *Nature Communications* **13**, 1 (2022).
- [55] M. Xie and S. D. Sarma, *arXiv*, 1 (2023), arXiv:2302.12284.
- [56] A. M. Clogston, *Physical Review Letters* **9**, 266 (1962).
- [57] B. S. Chandrasekhar, *Applied Physics Letters* **1**, 7 (1962).
- [58] G. Wagner, Y. H. Kwan, N. Bultinck, S. H. Simon, and S. A. Parameswaran, *arXiv* **0** (2023), arXiv:2302.00682.
- [59] Y. Z. Chou, F. Wu, and S. Das Sarma, *Physical Review B* **106**, 1 (2022).
- [60] A. Jimeno-Pozo, H. Sainz-Cruz, T. Cea, P. A. Pantaleón, and F. Guinea, *arXiv* (2022), arXiv:2210.02915.
- [61] G. Shavit and Y. Oreg, *Physical Review B* **108**, 1 (2023), arXiv:2303.04176.
- [62] L. Wang, I. Meric, P. Y. Huang, Q. Gao, Y. Gao, H. Tran, T. Taniguchi, K. Watanabe, L. M. Campos, D. A. Muller, J. Guo, P. Kim, J. Hone, K. L. Shepard, and C. R. Dean, *Science* **342**, 614 (2013).
- [63] A. A. Zibrov, C. Kometter, H. Zhou, E. M. Spanton, T. Taniguchi, K. Watanabe, M. P. Zaletel, and A. F. Young, *Nature* **549**, 360 (2017).
- [64] H. Zhou, T. Xie, A. Ghazaryan, T. Holder, J. R. Ehrets, E. M. Spanton, T. Taniguchi, K. Watanabe, E. Berg, M. Serbyn, and A. F. Young, *Nature* **598**, 429 (2021).
- [65] E. McCann and V. I. Fal'ko, *Physical Review Letters* **96**, 1 (2006).
- [66] J. Y. Khoo and L. Levitov, *Physical Review B* **98**, 1 (2018).

Supplementary information

This PDF file includes:

- Materials and Methods
- Band Structure Calculations
- Additional Notes on the Competing Order State
- Supplementary Figures

MATERIALS AND METHODS

Sample preparation: the bilayer graphene, monolayer WSe₂ (commercial source, HQ graphene) and hBN flakes for the van-der-Waals heterostructure are obtained by standard mechanical exfoliation of bulk crystals. The heterostructure is assembled via a dry transfer technique[62] using poly bisphenol a carbonate (PC) placed on a polydimethylsiloxane (PDMS) stamp. A dual graphite gated device design is chosen to reduce the charge disorder [63] and tune density n_e and displacement D field independently. The geometry of the device is then defined by a CHF₃/O₂ etch and contacted by ohmic edge contacts of Ti/Au (5nm/100nm). The BBG/WSe₂ sample and other devices of the same geometry were also studied in [8] for more information on sample preparation. For details on sample fabrication of the rhombohedral trilayer and Bernal bilayer graphene without WSe₂ measured in Fig. 4, see Ref. [1, 2, 64]. Sample 2 of Ref. [1] is used here to study BBG without WSe₂ support.

Transport measurements: Longitudinal resistance measurements are performed utilizing lock-in techniques at frequencies in the DC limit < 48 Hz and low currents of 1 - 2 nA. Each transport line is filtered by several Pi- and RC-filter stages at the mixing chamber and an additional RC filter with a cutoff < 5.7 kHz on the sample holder to reduce electronic noise and lower the electron temperature. We want to note that the present device has very long (> 10 μm) dual gated bilayer graphene contact leads (sample image see S14A) - compared to the many layer graphite contacts of devices used in previous studies[1]. Thus, the contacts are in the same phase as the bulk of the sample which has two consequences: first, contact resistances are a higher than for many layer graphite contacts of similar aspect ratio, leading to additional heating at the contacts. We attribute the saturation of resistance of SC₁ at the lowest temperatures to this heating effect (see Fig. 1D) while the disequilibrium of the charge carriers with the phonon bath simultaneously prevents efficient cooling. Second, the contacts become superconducting at much lower critical currents (corresponding to similar current *densities*) due to their long aspect ratio. In Fig. S14B, raw data is shown taken at $n_e = -7.3 \cdot 10^{11} \text{ cm}^{-2}$, $D = 1.15 \text{ V/nm}$ where T_c of SC₂ is maximal. The AC voltage drop across the sample and the DC current flowing through the sample is plotted against applied DC voltage bias. While the raw voltage drop follows typical behavior for a superconductor, the DC current shows two kinks without corresponding feature in the AC voltage data. These kinks can be explained by the superconducting transition of the dual gated bilayer graphene leads. As we calculate $R_{xx} = V_{AC}/I_{DC}$, such kinks visually imprint themselves onto the noise fluctuations of the zero resistance state—even in a four-terminal measurement setup. Therefore, features within the superconducting state such as in e.g. Fig. 2E or Fig. 4D should be disregarded as artefacts.

Shubnikov-de-Haas measurements: Magnetic field dependence of the longitudinal resistance of Fig. 2, S3 and S5 are taken with constant spacing in $1/B_{\perp}$ down to the lowest fields where quantum oscillation are visible. We perform Fourier transformations over different field ranges (see S4) sampled in $1/B_{\perp}$ and show the lowest field range in the main text for which all primary peaks of the quantum oscillations are clearly visible. This method reduces effects of higher harmonics and magnetic breakdown between different Fermi surfaces[42] (additional peaks in Fig. SS4C) and ensures that we can correlate our QO data with the zero field phase diagram. To convert gate voltages into charge density and normalize frequencies to the total Luttinger volume (as done in Fig. 2, S3 and S5), we calibrate the geometric capacitance of the gates to the sample via Shubnikov-de-Haas oscillations at zero displacement field and large densities. Further, a displacement field dependent voltage offset has to be accounted for. This voltage offset arises from that fact that the chemical potential has to be shifted out of the band gap of the BBG before increasing gate voltages is going to increase the charge carrier density. As transport and penetration field capacitance measurements are inaccurate in determining the exact position of the band edge in gate voltage space due to large resistances and long charging-times, we instead utilize the fully spin- and valley-polarized phase. Its frequency f_{ν} should be exactly one by definition, as all charge carriers live on a single Fermi surface. We adjust the voltage offset so that this is true over the whole gate voltage range of the quarter metal.

Field dependence: All measurements are performed in a dilution refrigerator with base temperature of $\sim 10 - 20$ mK and a 1T/1T/9T (XYZ) superconducting vector magnet. For the measurements of T_c domes vs B_{\parallel} , the sample is mounted with the field of the Z magnet aligned to the bilayer graphene plane and the out-of plane field component is carefully minimized to be < 0.1 mT using the XY magnets. T_c is determined for discrete in-plane fields as flux trapping in the XY magnets and field

misalignment of the Z magnet with the sample in this configuration prohibits continuous sweeping of B_{\parallel} while keeping $B_{\perp} \approx 0.0$ mT. Numerical values of T_c in Fig. 3 are extracted from fits of a step function to the raw data in fig. S6, S7, S8. We define T_c as the temperature when the resistance is half of its normal state value.

Penetration field capacitance: We utilize a capacitance bridge circuit to measure penetration field capacitance. In a previous capacitance bridge setup ([63]), a FHX35X high electron mobility transistor (HEMT) is directly connected to the sample gate, resulting in elevated electron temperatures above 100 mK. In order to lower the electronic temperature, we add an isolation capacitor made of silicon between the HEMT and the sample. We also installed a series of attenuators at each temperature stage to ensure thermalization of input coaxial cables. Finally, we added an ATF34143 HEMT at the 4K stage to transform the output impedance of the FHX35X HEMT and increase the bandwidth of output signal. (for full circuit schematic see Fig. reffig:S14).

We apply an A.C. excitation of $\sim 1 - 2$ mV and a frequency of 166.667 kHz. The improved capacitance setup described above allows us to measure inverse compressibility at the base temperature of our dilution unit. This can be best seen in Fig. 4B where transport and capacitance are measured simultaneously. Superconductivity is well developed in this case. This indicates no significant increase in the electron temperature; as a reference, T_c in BBG on hBN is less than 30mK. Indeed, R_{xx} linecuts with and without[1] simultaneous capacitance measurement show no noticeable difference.

BAND STRUCTURE CALCULATIONS

We computed the electronic dispersion $\epsilon_{\vec{k},j}$ and density of states $\rho(u, n_e)$ of BBG with layer-specific Ising spin-orbit coupling at interlayer potential $u = -100$ meV and electronic density n_e . The band structure of bilayer graphene without spin-orbit coupling is well-described near the K and K' points by a continuum model, expressed in the $(A1, B1, A2, B2)$ basis as [38, 65]

$$\mathcal{H}_0 = \begin{pmatrix} -u/2 & v_0\pi^\dagger & -v_4\pi^\dagger & v_3\pi \\ v_0\pi & -u/2 & \gamma_1 & -v_4\pi^\dagger \\ -v_4\pi & \gamma_1 & u/2 & v_0\pi^\dagger \\ v_3\pi^\dagger & -v_4\pi & v_0\pi & u/2 \end{pmatrix}, \quad \pi = \hbar(\xi k_x + i k_y), \quad v_i = \frac{\sqrt{3}a}{2\hbar}\gamma_i.$$

Here, $a = 2.46 \text{ \AA}$ is the monolayer graphene lattice constant and $\xi = \pm 1$ indicates whether \mathcal{H}_0 has been expanded about the $K = (\frac{4\pi}{3a}, 0)$ or $K' = (-\frac{4\pi}{3a}, 0)$ valley. We extract the band structure parameters from fits to quantum oscillation data (fig. S16). The hopping parameters are: $\gamma_0 = 2880$ eV for same layer hopping between nearest-neighbor sites, interlayer coupling term $\gamma_1 = 361$ meV for same effective hopping between dimer sites B_1 and A_2 , interlayer coupling term $\gamma_3 = 323$ meV for trigonal warping, and $\gamma_4 = 30$ meV for interlayer coupling between the dimer and non-dimer sites. Adding monolayer WSe₂ adjacent to one side of the bilayer graphene induces Ising SOC on the adjacent layer and can be accounted for in the model by adding a Hamiltonian \mathcal{H}_I [66]

$$\mathcal{H}_I = \begin{pmatrix} \xi\lambda_I\hat{s}_z & 0 & 0 & 0 \\ 0 & \xi\lambda_I\hat{s}_z & 0 & 0 \\ 0 & 0 & 0 & 0 \\ 0 & 0 & 0 & 0 \end{pmatrix}$$

acting on the A_1 and B_1 sublattices. Here, \hat{s}_z is a Pauli matrix acting on the spin subspace. The total Hamiltonian is then $\mathcal{H} = \mathcal{H}_0 + \mathcal{H}_I$. The electron density $n_e(\mu, u)$ at chemical potential μ and interlayer bias u is computed by evaluating

$$n_e(\mu, u) = \left(\frac{dk}{2\pi}\right)^2 \sum_{\vec{k},j} \frac{1}{\exp(\beta(\epsilon_{\vec{k},j} - \mu)) + 1}$$

where j indexes the energy bands and \vec{k} runs over the regular grid of momenta on which we computed the electronic dispersion $\epsilon_{\vec{k},j}$. The factor dk^2 normalizes for grid spacing. The electron density in Fig. 1 was evaluated at temperature $T = 10$ mK. The density of states $\rho(\mu, u)$ is computed by grouping the energy eigenvalues in bins of equal width dE and normalizing by bin size to be consistent with $dn_e/d\mu$.

T_c CALCULATIONS INCLUDING ORBITAL MAGNETIC FIELD

To include the orbital effect of in-plane magnetic field in the single-particle dispersion, we take $\vec{A} = z(\vec{B} \times \hat{z})$ and perform a Peierls substitution, which amounts to taking

$$\mathcal{H}_0(\vec{B}) = \begin{pmatrix} -u/2 & v_0\pi_+^\dagger & -v_4\pi_+^\dagger & v_3\pi \\ v_0\pi_+ & -u/2 & \gamma_1 & -v_4\pi_+^\dagger \\ -v_4\pi & \gamma_1 & u/2 & v_0\pi_-^\dagger \\ v_3\pi_+^\dagger & -v_4\pi & v_0\pi_- & u/2 \end{pmatrix}, \quad \begin{aligned} \pi_+ &= \xi(\hbar k_x + \frac{edB_y}{2}) + i(\hbar k_y - \frac{edB_x}{2}), & v_i &= \frac{\sqrt{3}a}{2\hbar}\gamma_i \\ \pi_- &= \xi(\hbar k_x - \frac{edB_y}{2}) + i(\hbar k_y + \frac{edB_x}{2}), & \pi &= \hbar(\xi k_x + ik_y), \end{aligned}$$

with d being the interlayer distance.

For simplicity, we consider a singlet pairing interaction local in the continuum (valley) description

$$\mathcal{H}_{\text{int}} = -V_s \int d^2r [\psi_+^\dagger(-is^y)\psi_-^\dagger][\psi_-(is^y)\psi_+],$$

where ψ_\pm is the 8-dimensional (spin, layer, and sublattice) vector of annihilation operators of a particle in valley $\xi = \pm 1$, and s_y is the second Pauli matrix in spin space. The gap equation is given by

$$\Delta_{\vec{q}} = \frac{V_s}{\Omega} \sum_{\vec{k}} \langle \psi_{\vec{k}+\vec{q}/2,-}(is^y)\psi_{-\vec{k}+\vec{q}/2,+} \rangle_{\Delta_{\vec{q}}},$$

where Ω is the system's area, and the expectation value is computed with respect to the mean field Hamiltonian \mathcal{H}_{MF} given below.

Denoting the transformation to band basis as

$$\psi_{\vec{k},\alpha,s,\xi} = \sum_n u_{n,\vec{k},\xi}^{\alpha,s} c_{n,\vec{k},\xi}, \quad \alpha = \{\sigma, l\} \text{ (sublattice and layer index),}$$

and neglecting inter-band pairing (justified due to the small SC gap at the vicinity of the transition), the mean-field Hamiltonian is given by

$$\mathcal{H}_{\text{MF}} = \sum_{n,\vec{k},\xi} \varepsilon_{n\vec{k}\xi} c_{n\vec{k}\xi}^\dagger c_{n\vec{k}\xi} - \Delta_{\vec{q}} \sum_{n,\vec{k},\alpha,s,s'} (u_{n,\vec{k}+\vec{q}/2,+}^{\alpha,s})^* (-is^y)_{s,s'} (u_{n,-\vec{k}+\vec{q}/2,-}^{\alpha,s'})^* c_{n,\vec{k}+\vec{q}/2,+}^\dagger c_{n,-\vec{k}+\vec{q}/2,-}^\dagger + \text{h.c.},$$

where

$$\Delta_{\vec{q}} = \frac{V_s}{\Omega} \sum_{n,\vec{k},\alpha,s} (u_{n,-\vec{k}+\vec{q}/2,-}^{\alpha,s}) (is^y)_{s,s'} (u_{n,\vec{k}+\vec{q}/2,+}^{\alpha,s'}) \langle c_{n,-\vec{k}+\vec{q}/2,-} c_{n,\vec{k}+\vec{q}/2,+} \rangle,$$

or in its linearized form

$$1 = \frac{V_s}{\Omega} \sum_{n,\vec{k}} |f_{n,\vec{k},\vec{q}}|^2 \frac{\tanh(\frac{\beta\varepsilon_{n,\vec{k}+\vec{q}/2,+}}{2}) + \tanh(\frac{\beta\varepsilon_{n,-\vec{k}+\vec{q}/2,-}}{2})}{2(\varepsilon_{n,\vec{k}+\vec{q}/2,+} + \varepsilon_{n,-\vec{k}+\vec{q}/2,-})}, \quad f_{n,\vec{k},\vec{q}} = \sum_{\alpha,s,s'} (u_{n,\vec{k}+\vec{q}/2,+}^{\alpha,s})^* (-is^y)_{s,s'} (u_{n,-\vec{k}+\vec{q}/2,-}^{\alpha,s'})^*.$$

It is important to note that the pairing potentials $\Delta_{\vec{q}}$ at different momenta \vec{q} are decoupled in the linearized gap equation. Thus, one can calculate $T_c^{(\vec{q})}$ for each momentum \vec{q} independently and take $T_c = \max_{\vec{q}}(T_c^{(\vec{q})})$. For finite in-plane magnetic field, time-reversal symmetry is broken, and therefore one really has to scan \vec{q} and cannot simply assume $T_c^{(\vec{q})}$ to be maximal for $\vec{q} = 0$. Generically, as one can expect, we find the optimal \vec{q} to point along the direction of $\vec{B} \times \hat{z}$.

In practice, to achieve results with high enough momentum resolution at a reasonable run time, we expand the non-interacting spectrum as

$$\varepsilon_{n,\vec{k}_F+\delta\vec{k},\xi}(\vec{B}) = \vec{v}_{n,\xi}(\vec{k}_F) \cdot \delta\vec{k} + \vec{\mu}_{n,\xi}(\vec{k}_F) \cdot \vec{B},$$

where \vec{k}_F is a point on the Fermi surface of the n^{th} band at $\vec{B} = 0$, $\delta\vec{k}$ is a vector pointing in the perpendicular direction from the Fermi surface, $\vec{v}_n(\vec{k}_F) = \vec{\nabla}_{\vec{k}} \varepsilon_{n,\vec{k}_F,\xi}$ is the Fermi velocity and $\vec{\mu}_{n,\xi}(\vec{k}_F) = \vec{\nabla}_{\vec{B}} \varepsilon_{n,\vec{k}_F,\xi}$ is the orbital magnetization of the Bloch state at a point on the Fermi surface labeled by \vec{k}_F .

ADDITIONAL NOTES ON THE COMPETING ORDER STATE

In the main text discussion of Fig. 3, we have noted a suppression of superconductivity at densities around $-6.9 \cdot 10^{11} \text{ cm}^{-2}$ and highest displacement fields. Here, additional data is shown in order to support and contextualize this argument and give further information about this "competing order state" (COS). First, the location of the COS is shown in Fig. S11 — only developing at high D above 1.05 V/nm for a small density range. A small out-of-plane magnetic field favors such state over SC_2 as indicated by the black arrows. Fig. S10A-D displays temperature and B_{\perp} dependence of SC_2 at $D = 1.15$ V/nm. Again, the COS appears at finite out-of-plane field and elevated temperatures with a characteristically increased resistance. It is useful to compare the energy scales of superconducting gap Δ and depairing energy E_D due to finite Cooper pair momentum. For a simple BCS superconductor, the superconducting gap is proportional to $k_B T_c$. An out-of-plane magnetic field breaks Cooper pairs due to their orbital motion at an energy that is proportional to $\sqrt{H_{c,2}}$. Thus, we contrast T_c^2 and $H_{c,2}$ plotted against density. Their density dependence agrees reasonably well within error, most notably in the region of the COS at $n_e \approx -6.9 \cdot 10^{11} \text{ cm}^{-2}$, see fig. S10C. Following this argument, not only T_c , but the superconducting gap is suppressed at these densities.

Non-linear transport reveals that COS is destroyed at finite current (Fig. S10E-G) with a critical temperature similar to T_c of SC_2 , reminiscent of a charge density wave state. Interestingly, the balance between COS and SC_2 is tipped in favor of superconductivity by lowering the magnetic field and temperature (Fig. S12). We also want to note that the fermiology evolves smoothly across COS (Fig. 2F) implying no additional symmetry breaking within the different isospin flavors. Instead, a natural explanation might involve nesting of different Fermi surfaces—only favored for wave vectors at specific densities.

SUPPLEMENTARY FIGURES

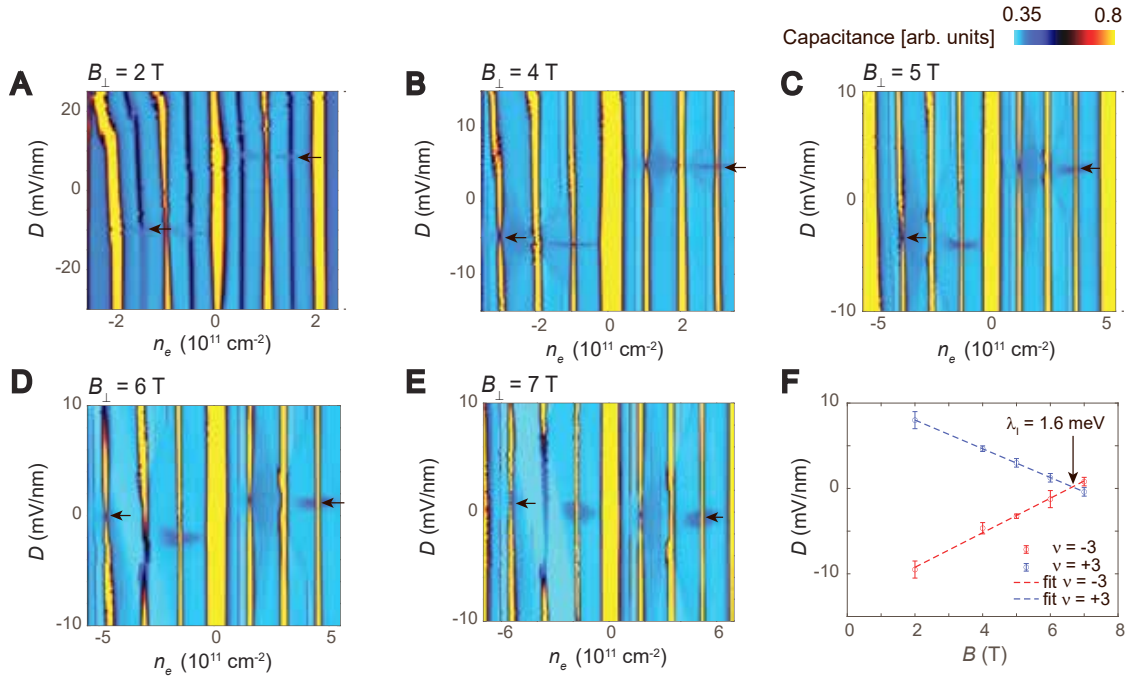


FIG. S1. **Measurement of Ising SOC from transitions in the lowest Landau level (LL):** (A - E) $D - n_e$ phase diagrams for different out-of-plane magnetic fields B_{\perp} at low displacement fields. The black arrows mark the orbital transitions of the $\nu = \pm 3$ LL used to determine the Ising SOC. (F) B_{\perp} dependent transitions plotted against D . The dashed lines are fits to the data. The Ising SOC is calculated from the crossing point of the $\nu = \pm 3$ lines[37]. Data from this device taken at higher temperatures and without in-plane magnetic fields was previously described in Ref. [8].

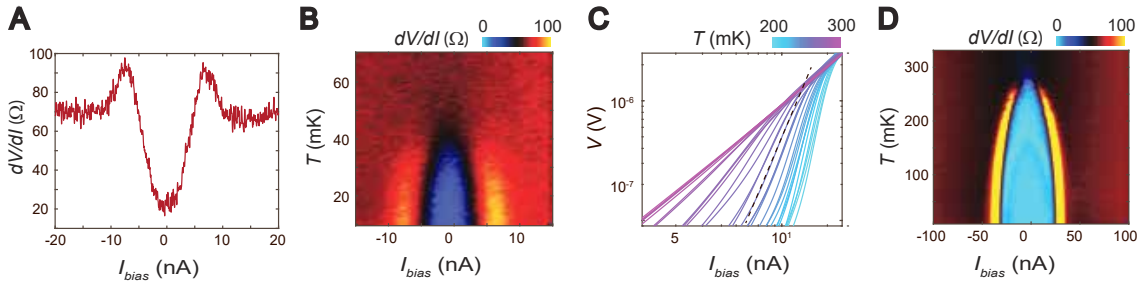


FIG. S2. **Additional bias and temperature dependence of SC_1 and SC_2 .** (A) linecut of the dV/dI spectrum of Fig. 1F at zero field and $n_e = -8.7 \cdot 10^{11} \text{ cm}^{-2}$ and $D = 0.95 \text{ V/nm}$. (B) Temperature dependence of panel A. (C) I-V characteristics extracted from temperature dependent non-linear transport data of SC_2 in (D) at $n_e = -7.3 \cdot 10^{11} \text{ cm}^{-2}$ and $D = 1.15 \text{ V/nm}$. The dashed line in C is a fit where $V \sim I^3$ which we define as the BKT-transition temperature.

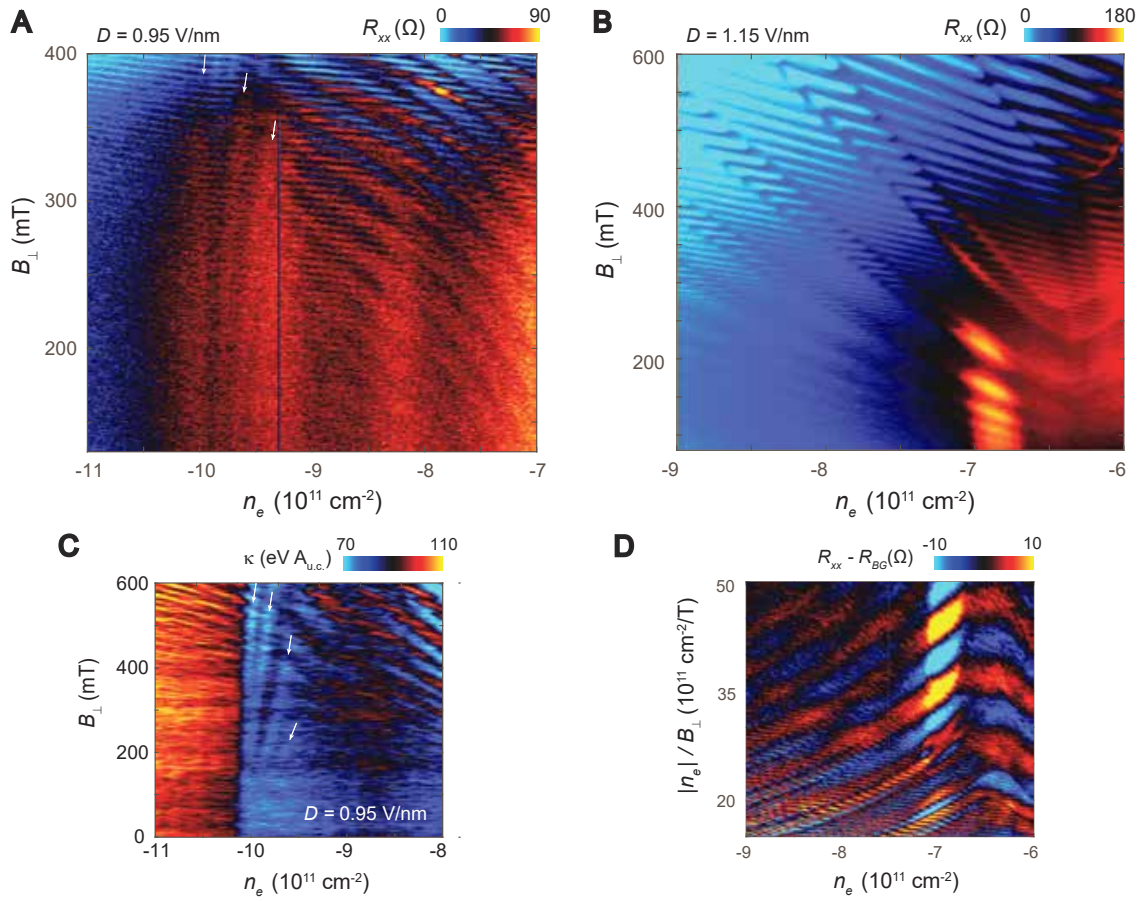


FIG. S3. **Raw quantum oscillation data.** (A - B) Shubnikov-de-Haas data taken at $D = 0.95$ V/nm and 1.15 V/nm, respectively. (C) B_{\perp} dependent inverse compressibility determined from penetration field capacitance data at $D = 0.95$ V/nm. The white arrows in A and C indicate the Landau fan associated with the small electron annulus in the $\text{Ising}_{2,2,-2}$ phase. (D) Same data as in panel B plotted as density n_e over B_{\perp} . An average background is subtracted from the raw data to visually enhance the quantum oscillations and illustrate no obvious change of quantum oscillations across the COS around $n_e = -6.9 \cdot 10^{11}$ cm $^{-2}$.

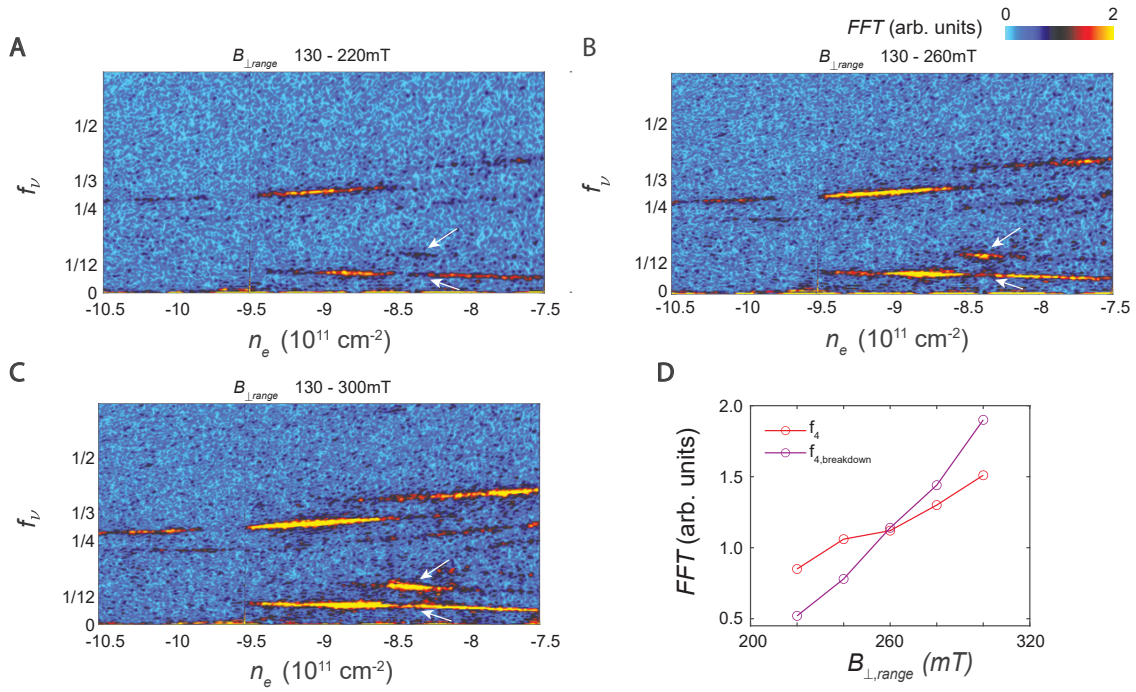


FIG. S4. **Magnetic breakdown between the small Fermi pockets.** (A - C) Fourier transformation of the data in Fig. S3A taken over different field ranges. The white arrows mark f_4 and $f_{4,breakdown}$. (D) Field range dependent FFT amplitude averaged over densities between $-8.49 \cdot 10^{11} \text{ cm}^{-2}$ to $-8.3 \cdot 10^{11} \text{ cm}^{-2}$. The relative weight between f_4 and $f_{4,breakdown}$ increases in favor of the latter for a larger and higher $B_{\perp,range}$, illustrating that $f_{4,breakdown}$ is due to magnetic breakdown between the fermi pockets associated with the frequency f_4 .

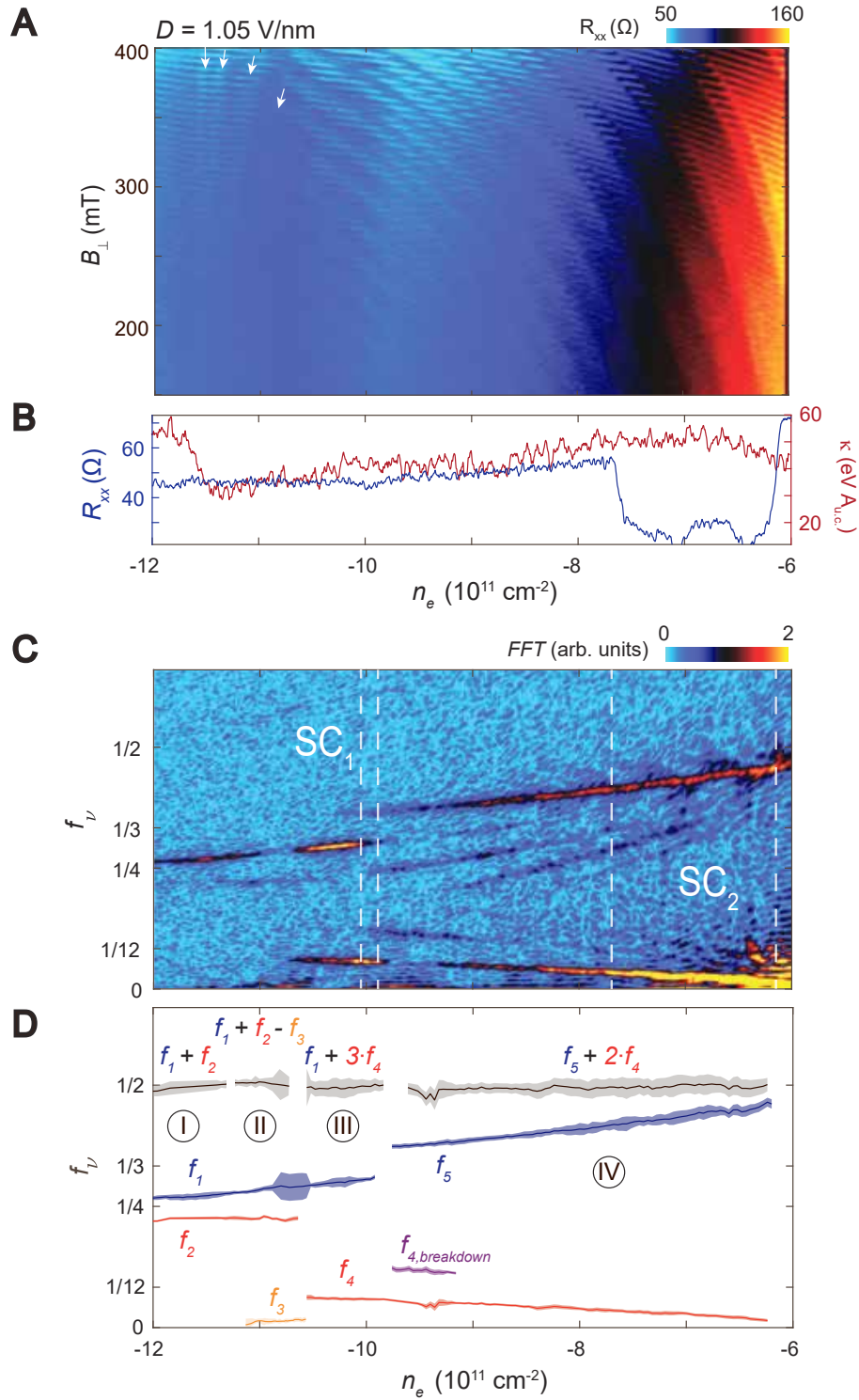


FIG. S5. **Shubnikov-de-Haas measurements and fermiology analysis at $D = 1.05 \text{ V/nm}$.** (A) raw quantum oscillation data which is used to compute the Fourier transform in panel C. The white arrows indicate electron like quantum oscillations associated with f_3 . (B) comparison of R_{xx} and inverse compressibility κ at zero magnetic field. (C) Fourier transform of the data in A for fields from 150 - 300 mT similar to main text Fig. 2B. The region of $SC_{1,2}$ are indicated by the white dashed lines. As SC_1 is not well formed and is barely visible in R_{xx} , one should confirm its location with the 2D resistance map in Fig. S13. Note: due to the higher field range used here compared to the main text, additional peaks associated with magnetic breakdown effects between different pockets of $f_{4,5}$ are apparent. (D) Schematic of panel C with main frequencies extracted via Gaussian fits to the data (f_3 is not well captured by fits and extracted manually here). The same phases as in the main text Fig. 2 are observed, most importantly showing the transition to the nematic $N_{2,4}$ phase.

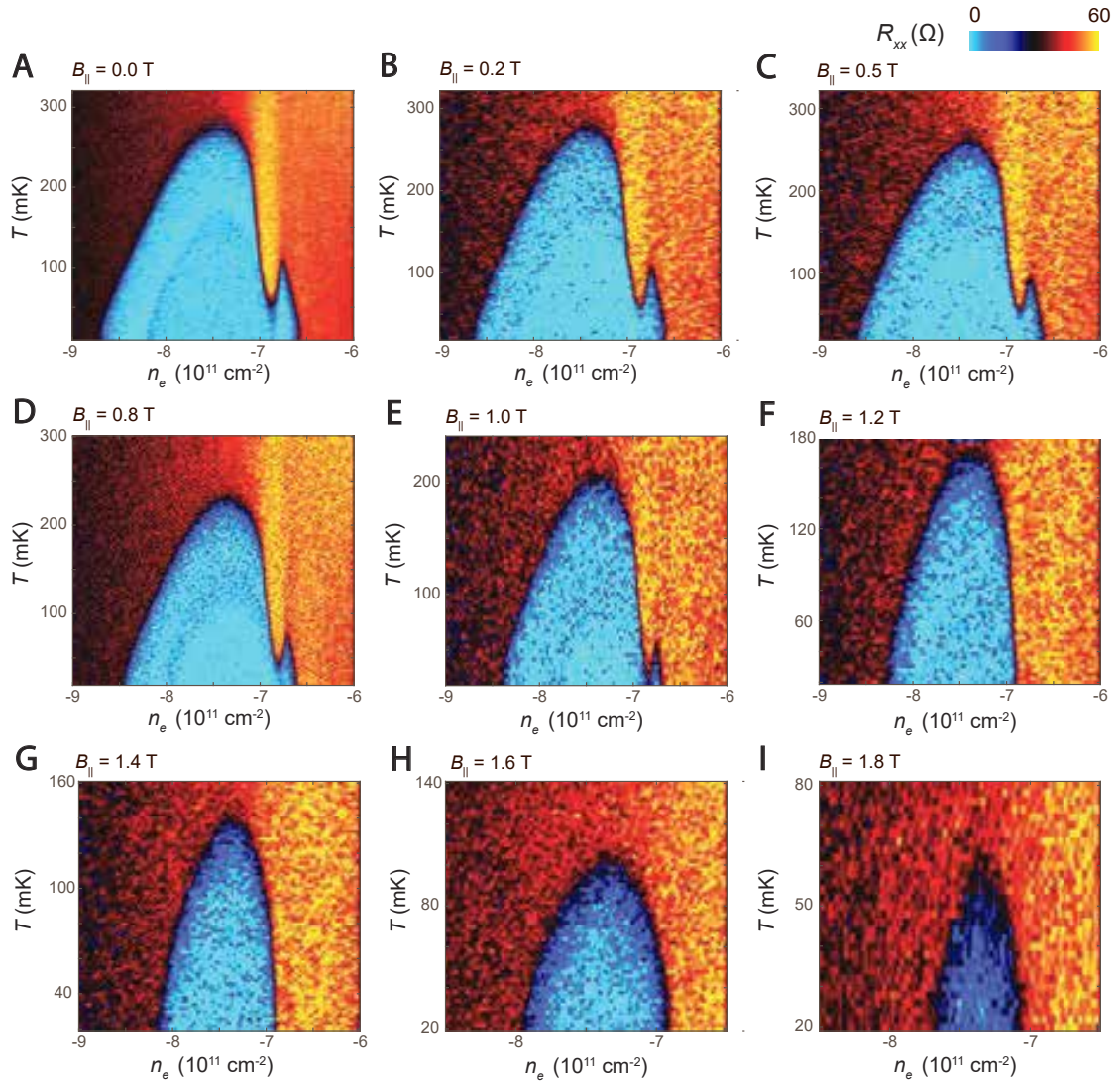


FIG. S6. In-plane field dependence of SC_2 at $D = 1.15 \text{ V/nm}$. (A - I) T_c domes for different in-plane magnetic fields B_{\parallel} up to 1.8 T.

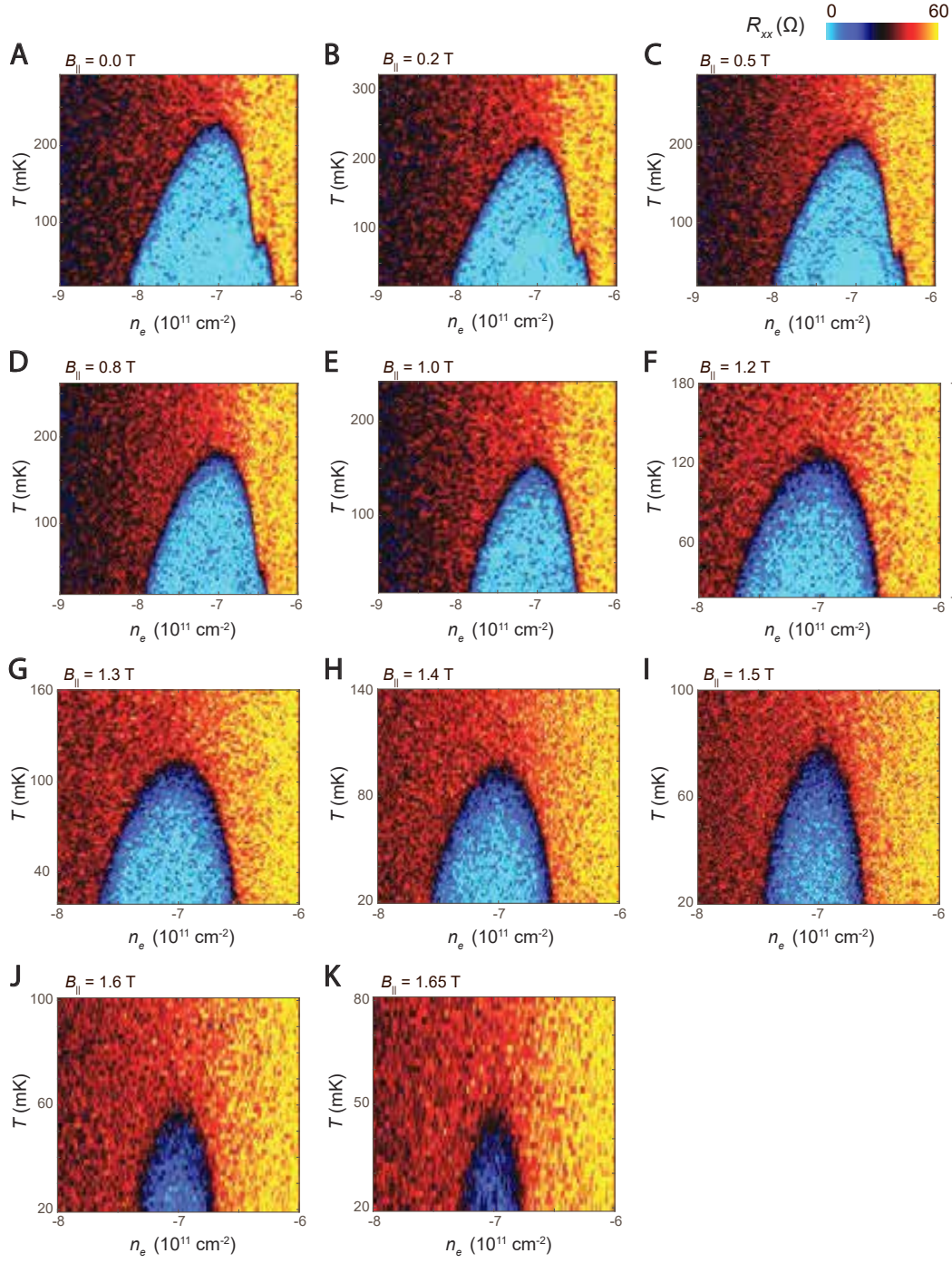


FIG. S7. In-plane field dependence of SC_2 at $D = 1.1$ V/nm. (A - K) T_c domes for different in-plane magnetic fields $B_{||}$ up to 1.65 T.

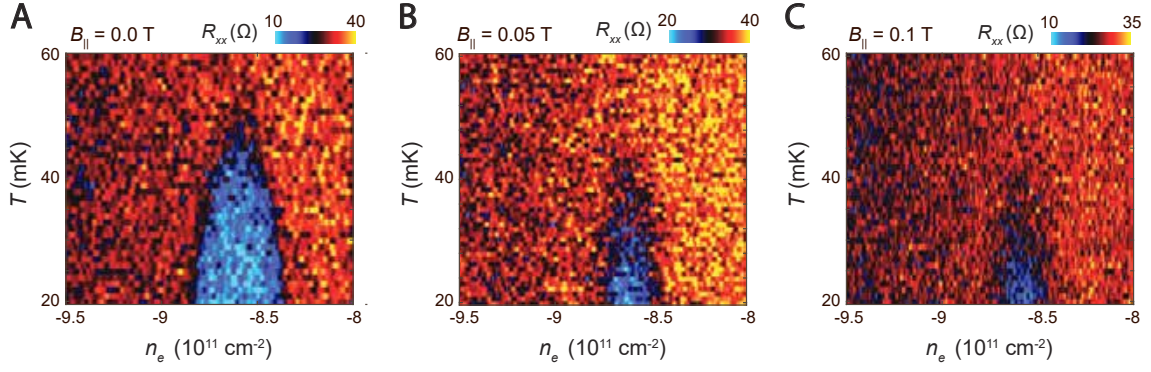


FIG. S8. In-plane field dependence of SC₁ at $D = 0.94$ V/nm. (A - C) T_c domes for different in-plane magnetic fields $B_{||}$ up to 0.1 T.

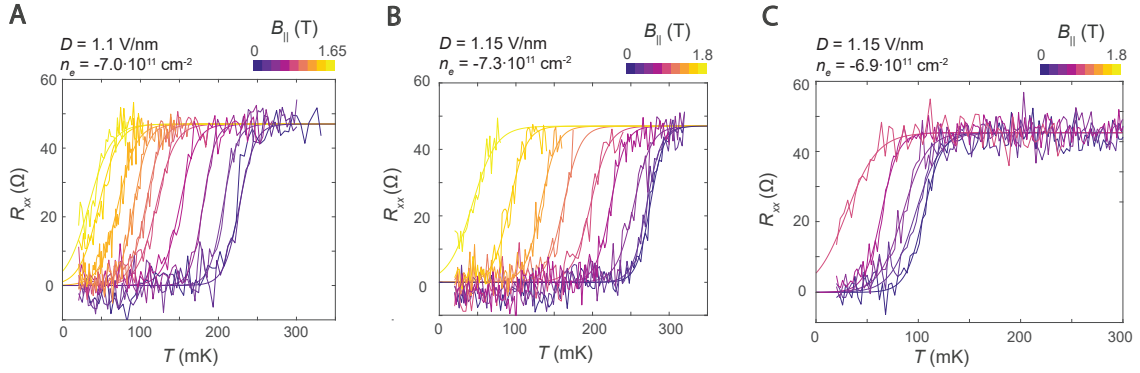


FIG. S9. Critical temperature extraction from superconducting domes. R-T linecuts of the data of fig. S6, S7, S8 from which in-plane field dependent critical temperatures are extracted. Both raw data and fits to the data are plotted. A-C display the three different n_e , D values. Experimental values in fig. 3 B are taken from panel B.

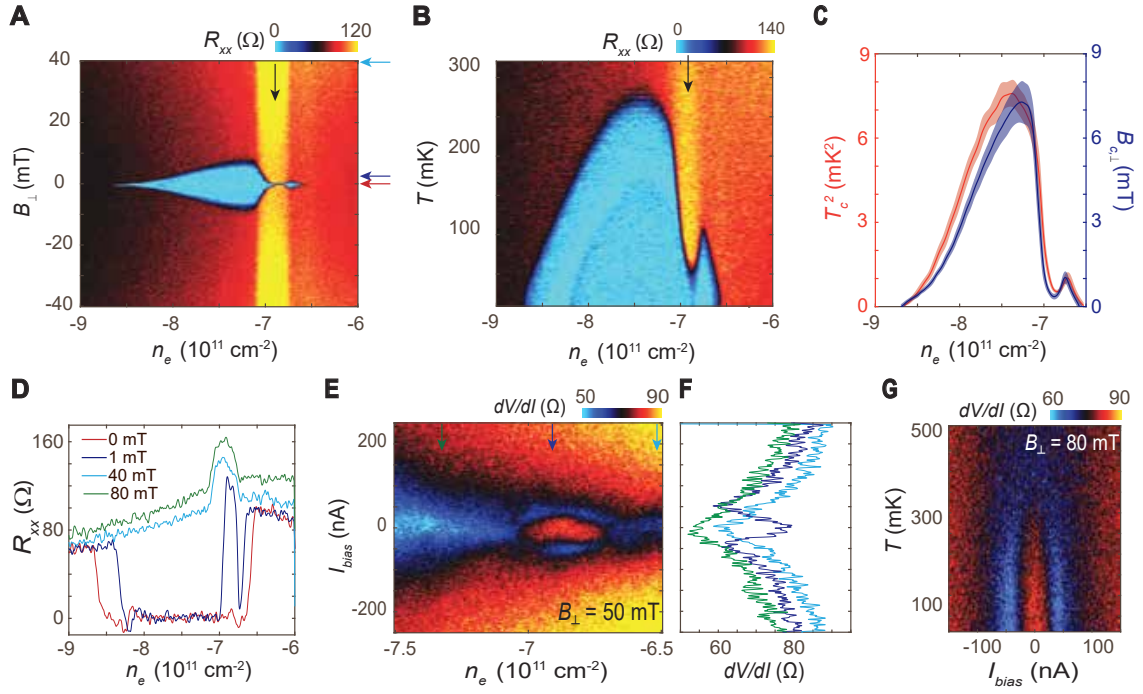


FIG. S10. **Competing phase in the superconducting regime.** (A) n_e and B_{\perp} dependence of SC_2 at $D = 1.15$ V/nm. (B) n_e and temperature dependence of SC_2 at the same displacement field. (C) Comparison of T_c^2 and $B_{c,\perp}$ extracted from fits to the data in A, B. Shaded regions represent error bars representing the width of the SC transition. (D) n_e linecuts of A for different B_{\perp} . (E) DC current bias dependence of COS. (F) Linecuts of E at the n_e values marked by the arrows in corresponding color. (G) Temperature - current bias dependence at $n_e = -6.95 \cdot 10^{11} \text{ cm}^{-2}$, $D = 1.15$ V/nm and $B_{\perp} = 80$ mT.

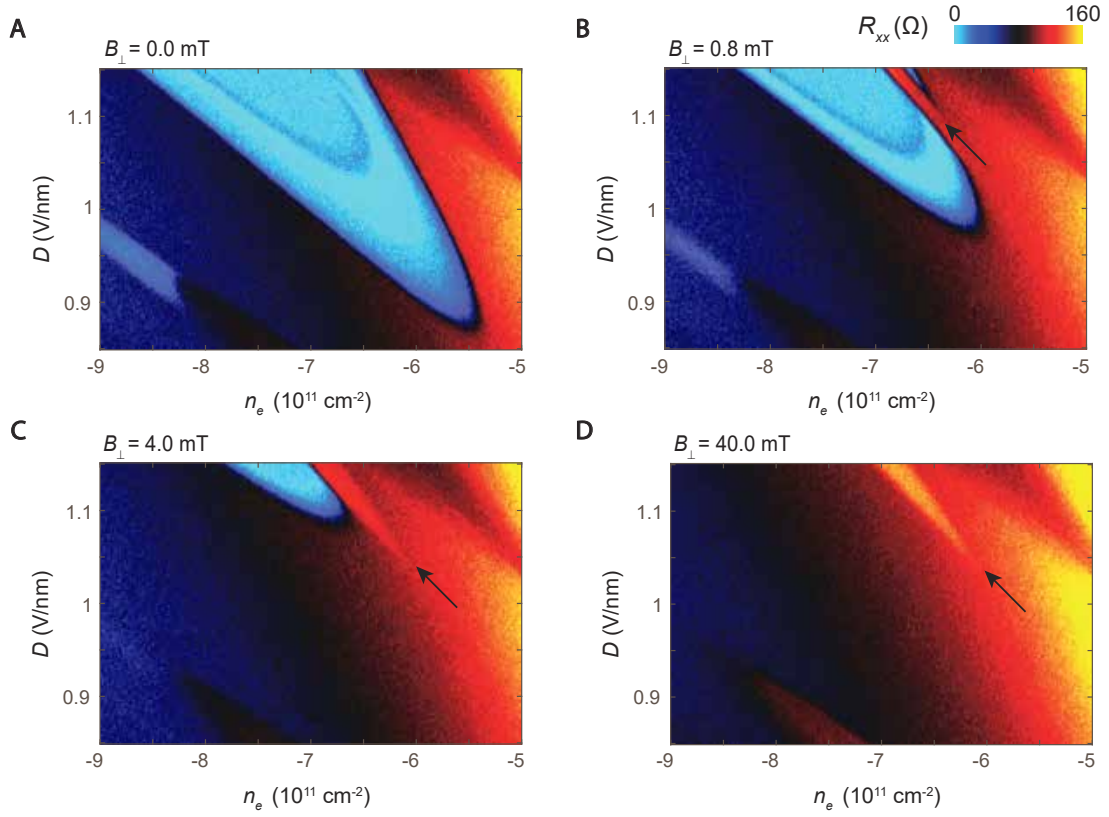


FIG. S11. **COS in the n_e - D phase diagram.** (A - D) phase diagrams for vanishing as well as small out of plane magnetic fields. Black arrows indicate the feature associated with the COS.

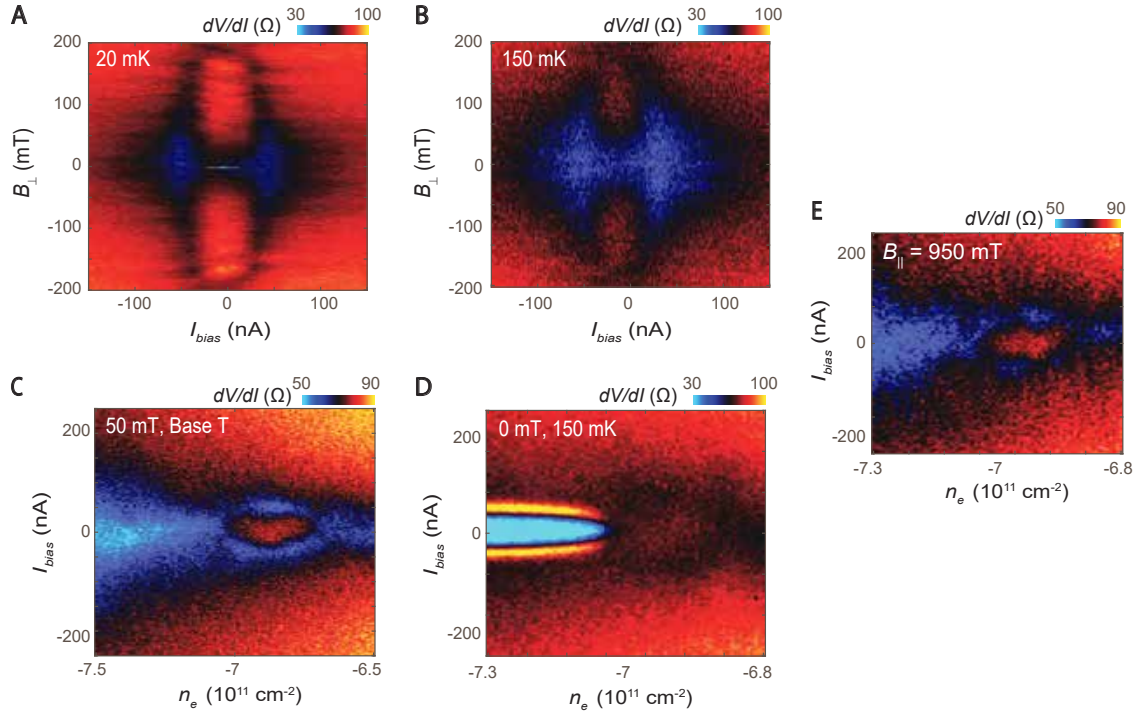


FIG. S12. **Additional data of the COS at $D = 1.15$ V/nm.** (A - B) Out-of plane field dependence of dV/dI and $n_e \approx -6.9 \cdot 10^{11} \text{ cm}^{-2}$ at base temperature and 150 mK. (C - D) Comparison of dV/dI at base temperature, $B_{\perp} = 50$ mT with $T = 150$ mK and $B_{\perp} = 0$ mT. E dV/dI at high in-plane field and $B_{\perp} = 50$ mT showing that COS is only weakly dependent on B_{\parallel} .

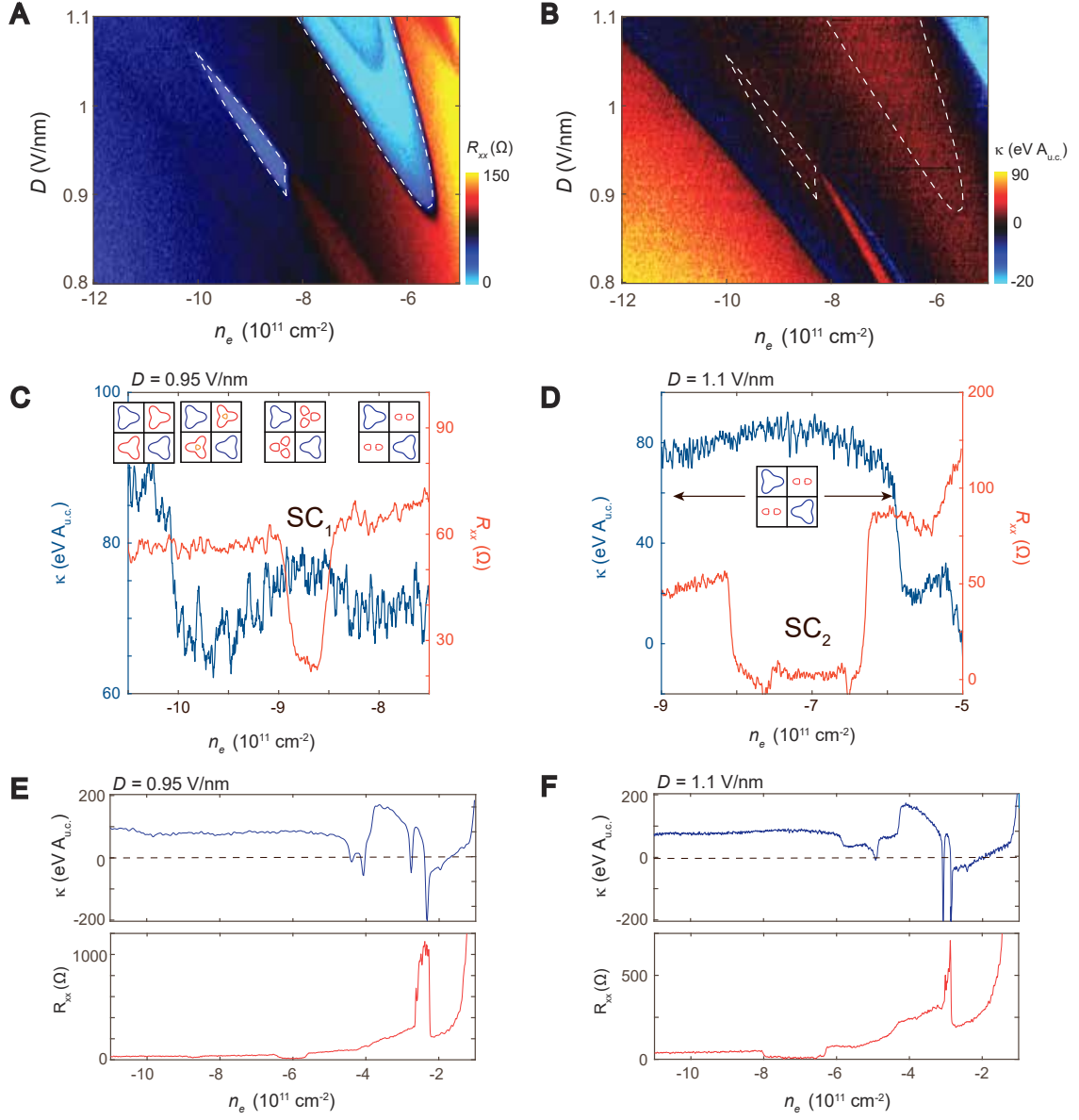


FIG. S13. **Comparison of transport and penetration field capacitance.** (A - B) n_e - D phase diagram of R_{xx} and κ over a larger density range than Fig. 4D, including SC_1 . The superconducting regions are overlaid from transport onto the inverse compressibility map via the white dashed line. (C) linecuts of R_{xx} and κ at $D = 0.95 \text{ V/nm}$ across SC_1 . The noise of κ gives an upper bound of $\sim 300 \text{ mK}$ on a possible chemical potential jump due to a first order phase transition below our experimental resolution. The fermiology is added as determined in Fig. 2. (D) same as Fig. 4C for a different $D = 1.1 \text{ V/nm}$. (E - F) κ (top panel) and R_{xx} (bottom panel) linecuts at $D = 0.95 \text{ V/nm}$ and 1.1 V/nm . At low $|n_e|$, several negative spikes in κ become apparent—illustrating the sensitivity of κ to first order phase transitions. The dashed lines marks zero as guide to the eye.

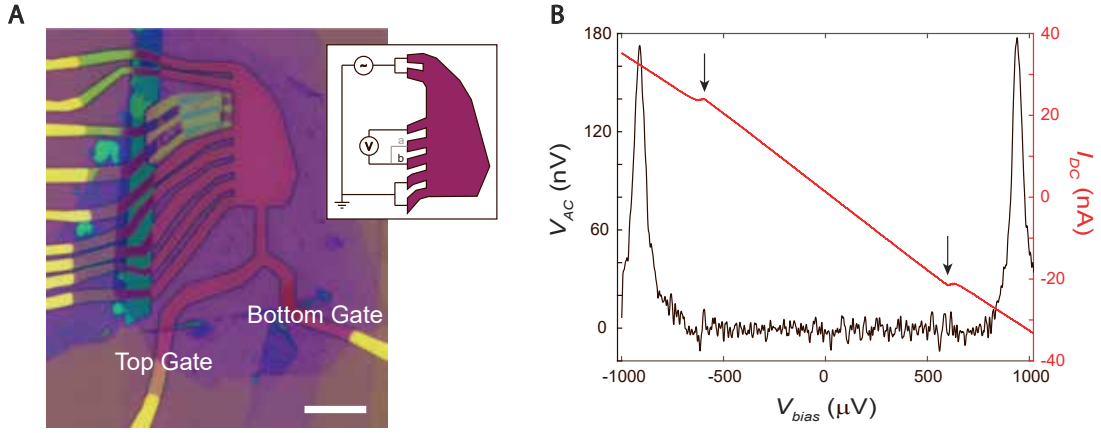


FIG. S14. **Sample image and raw data of the current-voltage characteristics of the superconducting state.** (A) image of the sample. The scale bar is $10 \mu\text{m}$. The inset shows the measurement setup used for transport measurements (contacts a and b are both used as negative voltage contact in different sets of measurements). (B) Voltage bias dependence of the raw voltage and DC current data at $D = 1.15 \text{ V/nm}$, $n_e = -7.3 \cdot 10^{11} \text{ cm}^{-2}$, deep within SC_2 . An AC-excitation of 1 nA is used to measure the voltage drop V_{AC} across the sample region while ramping the DC voltage bias, V_{bias} . The arrows indicate DC current jumps due to the superconducting transition of the dual gated bilayer graphene leads—uncorrelated with the voltage drop across the bulk of the sample.

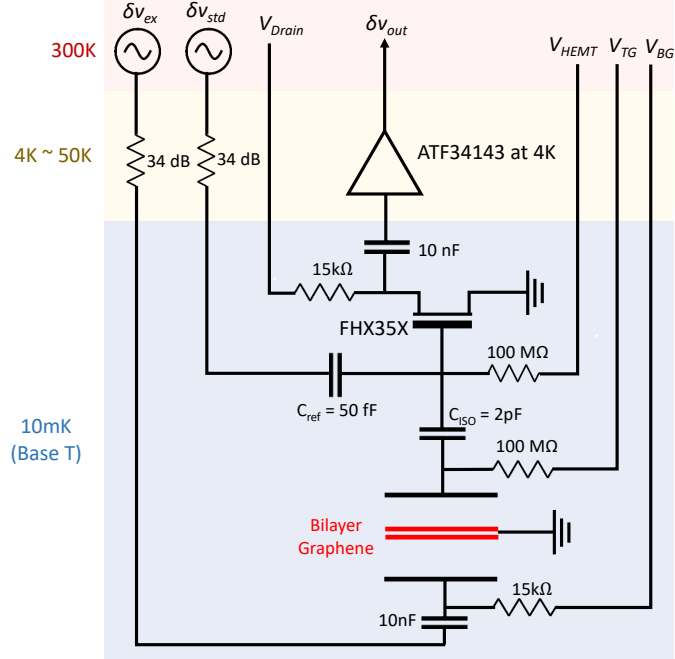


FIG. S15. **Circuit schematic of the penetration field capacitance measurements.**

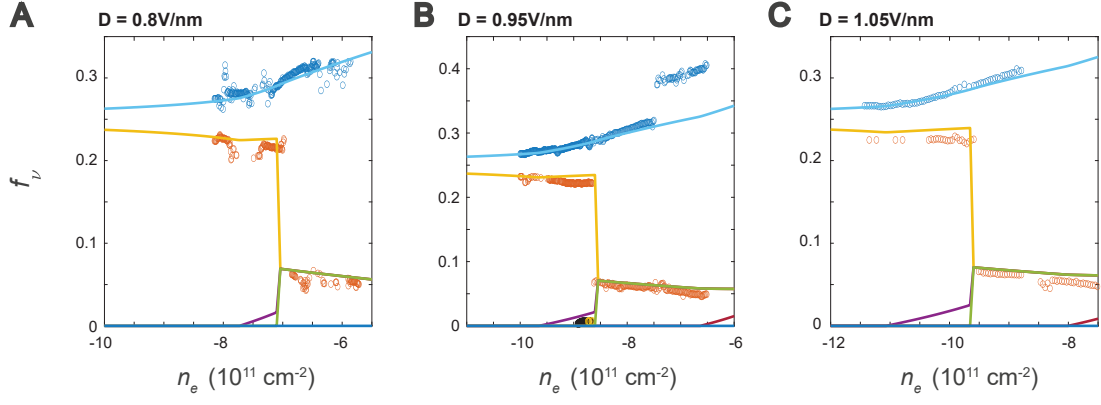


FIG. S16. **Bandstructure fits to quantum oscillations.** We find $\gamma_0 = 2880$ meV, $\gamma_1 = 361$ meV, $\gamma_3 = 323$ meV, $\gamma_4 = 30$ meV, $\delta = 13$ meV with Ising SOC set to $\lambda_I = 1.6$ meV from fits to single particle calculations. These values are used to calculate the in-plane orbital pair breaking.

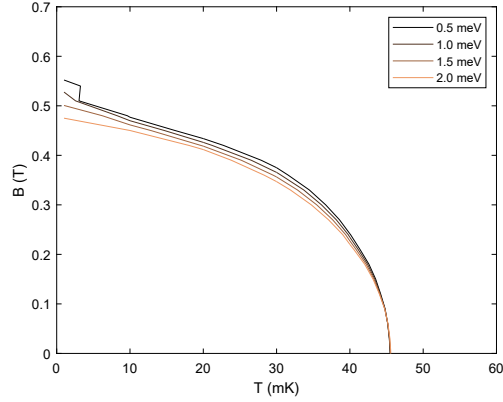


FIG. S17. **In-plane critical fields including orbital and Rashba SOC effects.** Analogous calculations to those of Fig. 3c of the main text, including both orbital depairing and the effect of Rashba spin orbit coupling with values ranging from from 0.5 - 2 meV.